Physics and Simulations in response to the DOE review for a Nosecone Calorimeter (NCC) for the PHENIX Experiment

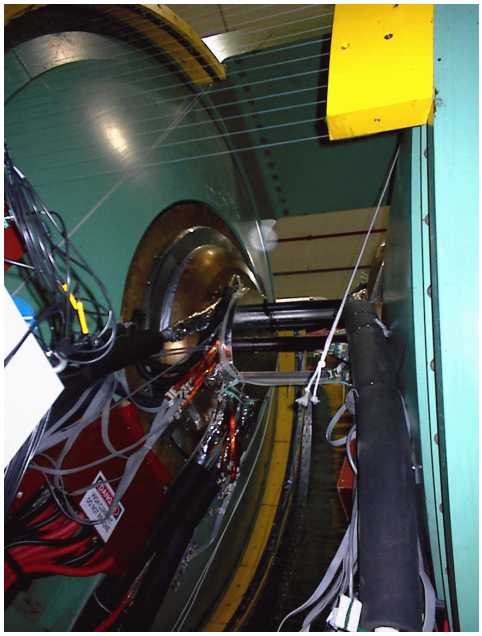

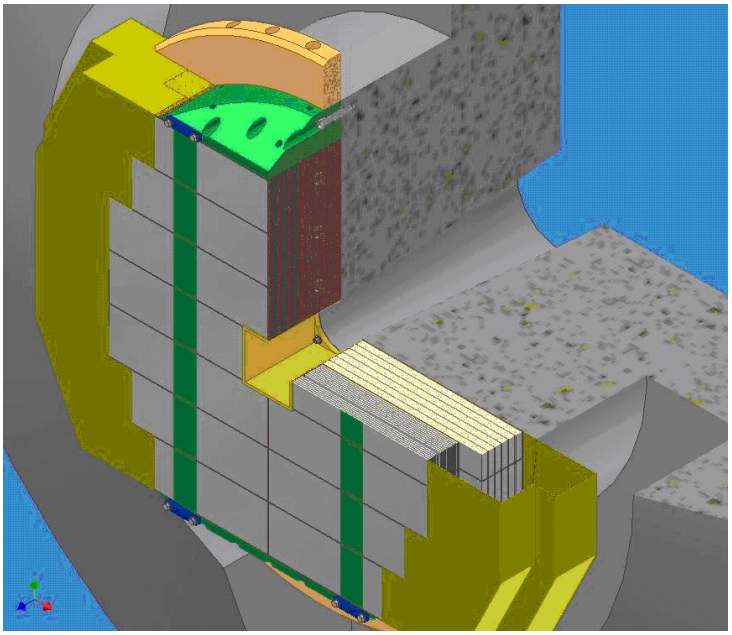

Relativistic Heavy Ion Collider
Brookhaven National Laboratory
March 5, 2008 version 2.2

PHENIX

PHENIX Nosecone Calorimeter

Participants

May, 2007

University of California, *Riverside, CA 92521, USA*
K. Barish, S. Bathe, P.S. Bourgeois, O. Chvala, T. Hester, M. Mendoza, A. Morreale, S. Rolnick, K. Sedgewick, R. Seto

Bhabha Atomic Research Centre *Trombay, Mumbai-400085, India*
R.K. Choudhury, A.K. Mohanty, P. Shukla, D. Dutta, P.K. Mukhopadhyay, A. Topkar

Instrumentation Dept., Brookhaven National Laboratory, *Upton, NY 11973-5000, USA*
Z. Li, V. Radeka, S. Rescia

Physics Dept., Brookhaven National Laboratory, *Upton, NY 11973-5000, USA*
S. Boose, M. Chiu, G. David, B. Johnson, E.P. Kistenev, D. Lynch, D. Morrison, R. Nouicer, R. Pak, R. Pisani, T. Sakaguchi, S.P. Stoll, A. Sukhanov, C. Vale, C.L. Woody

Charles University, *Ovocny trh 5, Praha 1, 116 36, Prague, Czech Republic*
Michael Finger, Miroslav Finger, M. Slunecka

Chonbuk University, *Chonju Chonbuk, 664-14, Korea*
J.B. Choi, E.J. Kim

University of Colorado, *Boulder, CO 80309, USA*
E. Kinney, J. Nagle

Columbia University and Nevis Laboratories, *Irvington, NY 10 533, USA*
C.Y. Chi

Czech Technical University, *Zikova 4, 166 36 Prague 6, Czech Republic*
M. Virius, T. Liska

Ewha Womans University, *Seoul 120-750, Korea*
I.S. Hahn, A. Kim, J. Lee, N.H. Lee, S.W. Nam, I.H. Park, J.S. Yoo

Florida State University, *Tallahassee, FL 32306, USA*
S. J. Edwards, A.D. Frawley

University of Illinois Urbana-Champaign, *Urbana, IL 61801, USA*
M. Grosse-Perdekamp, J. Koster, J.C. Peng

Institute of Physics, Academy of Sciences of Czech Republic, *Na Slovance 2, 182 21 Prague 8, Czech Republic*
P. Mikes, J. Popule, P. Ruzicka, L. Tomasek, M. Tomasek, V. Vrba

Iowa State University, *Ames, IA 50011, USA*
J.C. Hill, T. Kempel, J.L. Lajoie, F. Wei

Joint Institute for Nuclear Research- Dubna *Moscow Region, Russia*
S. Afanasiev, S. Bazylev, A. Baskakov, A. Bychkov, A. Cheremukhin, V. Elsha, N. Gorbunov, A. Isupov, N. Kotsev, A. Litvinenko, A. Malakhov, V. Peresedov, P. Rukoyatkin, V. Slepnev, I. Slepnev, N. Zamyatin, L. Zolin, E. Zubarev

University of Jyvaskyla/Helsinki Institute of Physics, *P.O.Box 35, FIN-40014, Jvyaskyla, Finland / P.O.Box 64 FIN-00014, Helsinki, Finland*
A. Kaskela, D.J. Kim, M. Oinonen, J. Rak, H. Steppänen

Korea University, *Seoul, 136-701, Korea*
B. Hong, H.H. Shim, K.S. Sim

Myongji University, *Yongin Kyonggido, 449-728, Korea*
K.S. Joo D.W. Kim, H.J. Moon

RIKEN, The Institute of Physical and Chemical Research, *Wako, Saitama 351-0198, Japan*
I. Nakagawa, A. Taketani

Skobeltsyn Institute of Nuclear Physics, Lomonosov Moscow State University, *Voro b'evy Gory, Moscow 119992, Russia*
G.A. Bogdanova, D. Karmanov, M. Merkin, V. Volkov, A. Voronin

Dept. of Physics and Astronomy, Stony Brook University, *SUNY, Stony Brook, NY 11794, USA*
A. Deshpande

Institute of Physics, University of Tsukuba, *Tsukuba, Ibaraki 305, Japan*
S. Esumi

Yonsei University, *Seoul 120-749, Korea*
J.H. Kang, Y. Kwon, S. Kim

Contents

Chapter 1

Executive Summary

This write-up is in response to the DOE scientific review of the NCC on July 9-10, 2007. In this document we address the following recommendations from the review report:

1. Each detector group should demonstrate and document scientific feasibility for two or more topics of high importance and submit to DOE for evaluation. PHENIX should submit to DOE a report documenting these studies for evaluation, prior to a technical review.

2. The NCC group should demonstrate by simulations that the non-projective geometry and shower digitization does not preclude the ability to eliminate background at the level necessary to accomplish the proposed physics goals. PHENIX should submit to DOE a report documenting these studies for evaluation, prior to a technical review.

The Nose Cone Calorimeter (NCC) is a compact tungsten silicon calorimeter covering 2π in azimuth and a pseudo-rapidity interval of $1 < \eta < 3$. The NCC, whose front face is located 41 cm from the nominal PHENIX interaction point, is approximately disk-shaped, 19 cm thick with a radius of 50 cm. It is composed of tungsten absorbers interleaved with silicon sensor pads and configured in three longitudinal sections, EM1, EM2 and HAD. The tungsten plates in EM1 and EM2 are 4 mm thick while the absorber in the HAD section is 11 mm thick. The silicon is segmented into $15\times15\,\mathrm{mm}^2$ pads in order to match the Molière radius of the device. In addition, EM1 contains two layers of finely segmented 2-D readout silicon strip layers for shower separation located at depths of $2\,\mathrm{X}_0$(radiation lengths) and $3\,\mathrm{X}_0$. We call these Photon Identifier 1 and 2 (PI1 and PI2). The thicknesses of EM1, EM2 and HAD, as well as the positions of PI1 and PI2, have been optimized since the TDR. The thicknesses of the EM1, EM2 and HAD towers are $8\,\mathrm{X}_0$, $8\,\mathrm{X}_0$, and $19\,\mathrm{X}_0$, respectively. The NCC parameters can be found in Table 1.1.

The Nose Cone Calorimeter is designed to work as a tracking calorimeter and as such is non-projective in the same sense that a coarsely pixelated tracking chamber is non-projective: hits on each plane of the detector are associated with hits in other planes to form tracks. EM1, EM2, and HAD serve as the three tracking planes of the NCC (Figure 2.2) Tracks deposit energy in multiple towers of each longitudinal plane to form clusters or "hits". Hits in each of the three planes are then associated with one another to form tracks. This design

Table 1.1: Nose Cone Calorimeter design parameters

Parameter	**Value**	
Distance from collision vertex	41 cm	
Radial coverage	50 cm	
Absorber	W ($35\,X_0$ or $1.3\,L_{abs}$)	
Readout	Si pads ($15\times15\,mm^2$) in calorimeter and strips (0.5x60 mm^2) in photon identifier	
Calorimeter Sampling Layers	EM1 and EM2: 7 sampling layers (4 mm W + 0.5 mm Si) each HAD: 6 sampling layers (11 mm W + 0.5 mm Si)	
Photon identifier (PI) Layers	2 X/Y strip layers (0.3 mm Si) downstream of second and third EM sampling layers	
Si sensors	Pad structured	3320 ($14\times160 + 6\times180$)
	Strip structured	640 (4×160)
Channel count	Calorimeter	8000
	Photon identifier	81920 (672 SVX4 chips)
Estimated EM energy resolution	$23\%/\sqrt{E} + 1\%$ at a normal impact	
Two showers resolved at	3 cm	in calorimeter
	2 mm	in photon identifier

gives a reasonably uniform (to within 20%) probability of finding electromagnetic showers for all angles, for rapidities between 1 and 2.5 and shower energies between 1 and 40 GeV (Fig. 2.7 and Fig. 2.8). In central Au+Au events, at rapidities above 1.5, the efficiency for lower energy showers (below 5 GeV) drops due to overlapping showers.

After tracks are found, further assembly is an iterative process of incorporating hits into the tracks to form a shower (which we continue to call "track"). Longitudinal and transverse χ^2s are associated with each track and used for identifying whether the track was an electromagnetic shower, a MIP track or a hadronic shower. In addition, the two layers of strip detectors PI1 and PI2, with 50 μm pitch, are used to identify whether a track results from a single photon or two photons. If it is found to contain two photons, the ADC values in the strips are used to find their energy asymmetry. Using the total energy, energy asymmetry and opening angle (again taken from PI1 and PI2), one can reconstruct the invariant mass of the two overlapping showers.

We have chosen to illustrate the capabilities of the NCC by doing full simulation studies of: 1) π^0 R_{AA} in heavy ion collisions and its implications for the measurement of direct photons and photon+jet events and 2) R_{AA} for χ_C as measured by its decay into $J/\psi + \gamma$ in heavy ion collisions. These physics signatures are among the most critical to make and will give insight into the properties of the sQGP, in particular on the mechanisms of energy loss

and deconfinement.

The simulations start from the generation of signal events and background (HIJING for Au+Au and d+Au, PYTHIA for p+p) and are run through a full GEANT Monte-Carlo (PISA) for which we have included the NCC as a new subsystem. The events are then simulated through the electronics chain, using a detector response model (consistent with the 14 bit digitization which we will be using and for which we have a working prototype) and full reconstruction. Figure 1.1 shows a schematic flowchart of the steps taken. After

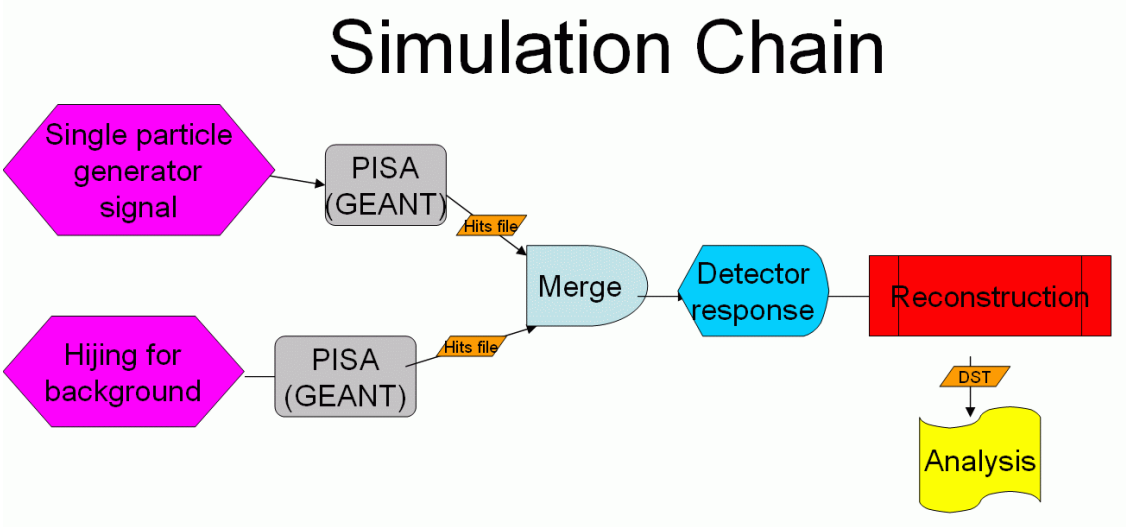

Figure 1.1: Flowchart of the steps used in these simulations.

reconstruction the data is then analyzed to yield the appropriate signals we wish to explore. We briefly outline the analysis steps to reconstruct π^0s which form the core of our R_{AA} π^0 analysis, as well as the steps for χ_C simulation and analysis.

π^0 analysis Two techniques are used to reconstruct π^0s. For energies below about 5 GeV, the standard method of forming the invariant mass of all pairs of photons with energy greater than 0.5 GeV is used. We call these "two-track" π^0s. Cuts on the longitudinal and lateral χ^2 were imposed on each photon. The opening angle between the two photons was required to be greater than 50 mr and the energy asymmetry was required to be less than 0.8, i.e. $((E_1 - E_2)/(E_1 + E_2) < 0.8$ where E_1 and E_2 are the energies of the two photons. The latter cut removes much of the background where a higher energy shower is combined with a very low energy shower. The background subtraction was done using mixed events. In the case of Au+Au events we limited the rapidity to η <1.5 GeV, in order to reduce the effect of occupancy (Fig. 1.2 shows the regions of rapidity in which various physics signatures will be accessible in the NCC). For higher energy π^0s the two photons overlap. In order to identify such showers as π^0 candidates, the strip detectors PI1 and PI2 were used to obtain an opening angle and energy asymmetry. This information together with the total energy in the shower was used to form an invariant mass. A cut of 135±50 MeV is applied to the resulting mass to select π^0 candidates; these are referred to as "single track" π^0s. Each candidate is asssigned

a weight giving the probability that it is a π^0. The spectra and nuclear modification factors, R_{AA}, are obtained for both single track and two track π^0s under the assumption of RHIC-II luminosity for a 10 week run. The simulation study is used to calculate the error bars, which are plotted on an assumed R_{AA} value to illustrate the sensitivity of the measurement.

χ_C analysis The χ_C is reconstructed via its J/$\psi+\gamma$ decay mode where the J/ψ is detected through its dimuon decay mode in the existing muon spectrometer located just behind the NCC. For the simulation, a mixture of J/ψs and χ_Cs were thrown, where the relative composition is consistent with the known feed-down of J/ψ from χ_C in p+p collisions. The background under the J/ψ peak in the dimuon invariant mass distribution was taken from measurements with the present PHENIX data. We assumed a factor of 2.5 improvement in S/B for the J/ψ from the FVTX. This arises from an improvement in mass resolution, and in the rejection of muons from hadron decay [1]. These events were then embedded into background events, and the reconstruction packages for the muon spectrometer, the FVTX, and the NCC were run. The J/$\psi + \gamma$ invariant mass was then formed where the γ was required to have E_γ >0.5 GeV and a longitudinal χ^2 consistent with being a electromagnetic shower. As in the case of the two-track π^0s, a mixed event technique was used to obtain the background shape. An opening angle cut was made between each of the muon tracks and the photon. Again, for central Au+Au collisions we limited the analysis to η <1.5, see Fig. 1.2.

A short summary of the results follows:

- The reconstruction efficiency as a function of angle, momentum, and multiplicity is reasonably uniform – this tells us that the the design of a non-projective tracking calorimeter and shower digitization capabilities of the NCC are sufficient to detect relevant signals, and the capability to eliminate background is appropriate to accomplish the proposed physics goals.

- The π^0 cross section and R_{AA} will be measured between transverse momenta of 1 and 20 GeV, allowing us to determine R_{AA} at 15 GeV to better than 20 %. At lower energies

NCC physics signatures			
	π^0 2-track	π^0 Single track	χ_C
pp	E<6 GeV 1<Y<2.5	E>6GeV 1<Y<2.5	1<Y<2.5
dAu	E<6 GeV 1<Y<2	E>6GeV 1<Y<2.5	1<Y<2.5
AuAu mid-central	E<6 GeV 1<Y<2	E>6GeV 1<Y<2.5	1<Y<2
AuAu central	E<6 GeV 1<Y<1.5	E>6GeV 1<Y<2.5	1<Y<1.5

Figure 1.2: Summary of rapidity coverage for each physics signal studied.

below about 10 GeV, statistics is much higher and R_{AA} will be measured to within a few percent – a precision which should allow us to discriminate between models of energy loss (Fig. 3.3.3). The π^0 analysis forms the foundation of our direct photon analysis.

- The R_{AA} of the χ_C in heavy ion collisions can be measured to within 10 % up to an N_{part} of about 250 – sufficiently well measured so that together with the J/ψ and ψ' data one can significantly constrain models of charmonium suppression and distinguish between various models of deconfinement (or other means of dissociation) and regeneration (Fig. 3.16).

Chapter 2

The NCC: principles of design and operation

A remarkable result has emerged from the first several years of data taking at RHIC – the high temperature and density phase of QCD matter created in heavy ion collisions at RHIC is best described as a near perfect fluid – the strongly interacting Quark-Gluon-Plasma (sQGP). This state is characterized by a small viscosity to entropy ratio, and a high density of color charges which induce huge energy losses in partons traversing the medium. The task for the future is to understand the characteristics of the sQGP, and perhaps more importantly – to gain some insight into how and why such a medium is created. Many of the important scientific discoveries and associated publications at RHIC benefited enormously from the contribution of the PHENIX Central Arm calorimeters, see [2, 3, 4, 5, 6, 7, 8, 9, 10, 11, 12], to name a few references. The coverage of the present PHENIX electromagnetic calorimeter is rather limited, covering half the azimuth and -0.35$< \eta <$0.35. Advances in the understanding of this fundamental state of matter would be facilitated by a larger coverage with high resolution electromagnetic calorimetry, both to increase the rate for low cross section phenomena, and to cover a broader range of pseudorapidity, in order to study the rapidity dependence of the medium's properties. For this reason we are proposing to construct and add the NCC to the PHENIX suite of detectors.

Our prime motivation is to provide precision measurements of direct photons, π^0s and jets as well as the χ_C over an extended range of rapidity in A+A, (p)d+A, and polarized p+p collisions. This upgrade will provide access to physics observables that are not currently accessible to PHENIX or that are now available only indirectly and with very limited accuracy.

2.1 The NCC design: a tracking calorimeter

The second of the recommendations of the review report stated:

- The NCC group should demonstrate by simulations that the non-projective geometry and shower digitization does not preclude the ability to eliminate background at the

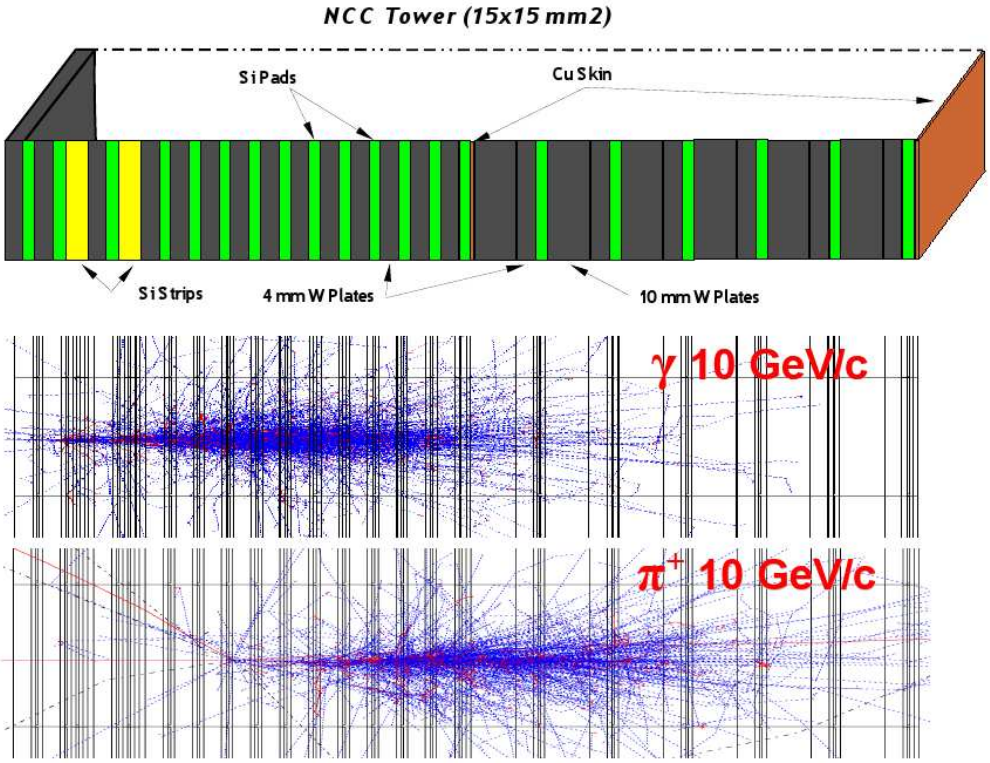

Figure 2.1: Longitudinal structure of a single calorimeter tower showing the locations of the three calorimetric segments, EM1, EM2, and HAD, and the high-resolution position sensitive layers. Shown in the bottom panel are electromagnetic and hadronic showers due to a 10 GeV/c photon and a charged pion of the same energy.

> level necessary to accomplish the proposed physics goals. PHENIX should submit to DOE a report documenting these studies for evaluation, prior to a technical review.

We will answer this question in the next few sections of this document.

The NCC is a highly segmented tracking calorimeter designed to reconstruct and identify electromagnetic signals at intermediate rapidities in close proximity to the production vertex. This detector takes full advantage of the large body of existing data on particle showering in matter to design a total absorption calorimeter that is able to measure the energy and direction of impinging particles and to discriminate between electromagnetic and hadronic showers. The NCC is composed of two identically structured high density fine sampling electromagnetic segments (EM1 and EM2) and one coarse hadronic (HAD) segment. EM1 also houses two layers of high resolution two-dimensional position sensitive detectors, at optimal depths of $\sim 2X_0$ (L1) and $\sim 3X_0$ (L2). The role of the position sensitive detectors PI1 and PI2 is to count photon hits, measure hit-to-hit separation and estimate the energy sharing between possible contributors to high energy tracks built of clusters seen in calorimeter segments. The longitudinal structure of the calorimeter tower is sketched in Fig. 2.1.

The NCC is located 41 cm from the nominal collision point, on the poles of the PHENIX central magnet, and limited to a depth of 19 cm. It is built of tungsten plates (4 mm thick

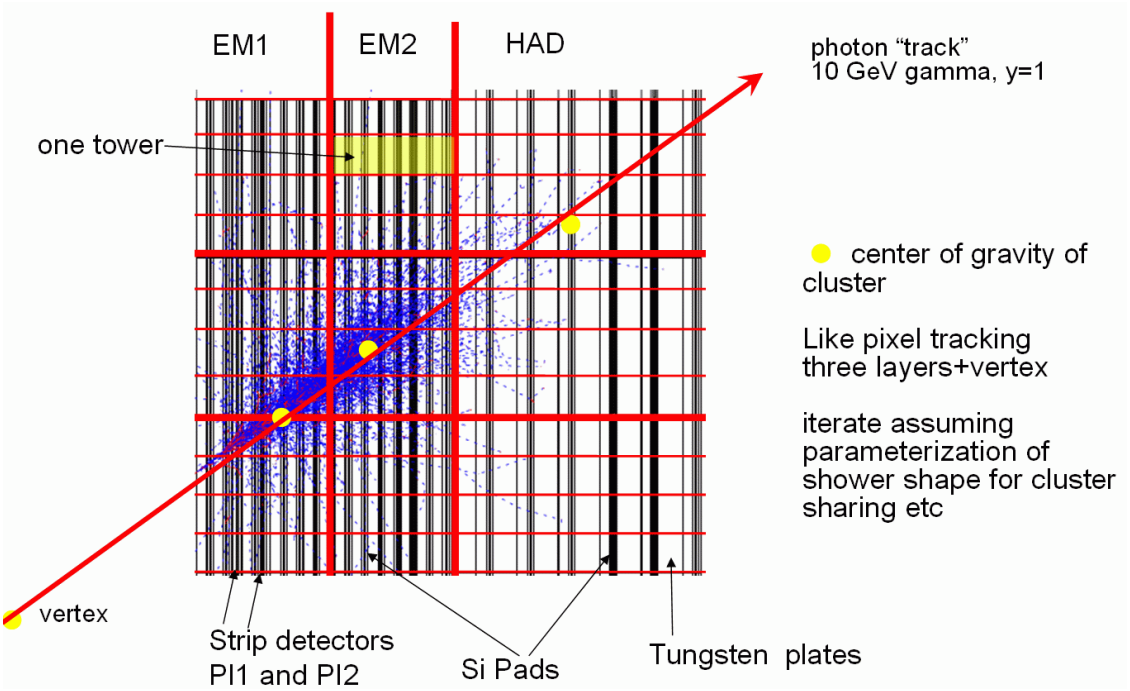

Figure 2.2: Principles of tracking measurements in the NCC. Linking the centers of gravity of the clusters found in each section provides tracking information without projective geometry, as illustrated.

in EM1 and EM2 and 11 mm thick in the HAD segment) interleaved with silicon readout layers. The readout layers are structured into pads of $15 \times 15\,\mathrm{mm}^2$ in the calorimeter and strips of $0.5 \times 60\,\mathrm{mm}^2$ in the position sensitive layers. EM1 and EM2 together are 16 L_{rad} deep; the hadronic segment adds an additional $19\,L_{rad}$ to the total depth of the NCC. The Molière radius of the NCC is approximately 14 mm.

An extensive set of performance measures based upon a standalone simulation chain implementing a free standing NCC in GEANT3 was published as part of the NCC CDR. The NCC has since then been integrated into the complete PHENIX GEANT simulation, which includes all material located in PHENIX, allowing for the study of all aspects of running the NCC as part of the PHENIX experiment. The pattern recognition algorithms were further refined to optimize energy and position resolution, along with efficiency and sensitivity to shower shape measurements. The new and largely improved suite of software has been used to provide answers to the questions generated as a result of the NCC Science review in July 2007.

By design, the NCC segments are structured into mechanically non-projective towers (see Fig. 2.2). This NCC design feature was prompted by the existing experience with the PHENIX central calorimeters. There we have particles hitting at angles up to 20° without any noticeable effect on the calorimeter's performance. The towers in EM1 and EM2 have an aspect ratio of ∼2 (ratio of the tower depth to its lateral size measured in the diagonal direction). The mechanical aspect ratio increases by a factor of 2 in the hadronic segment

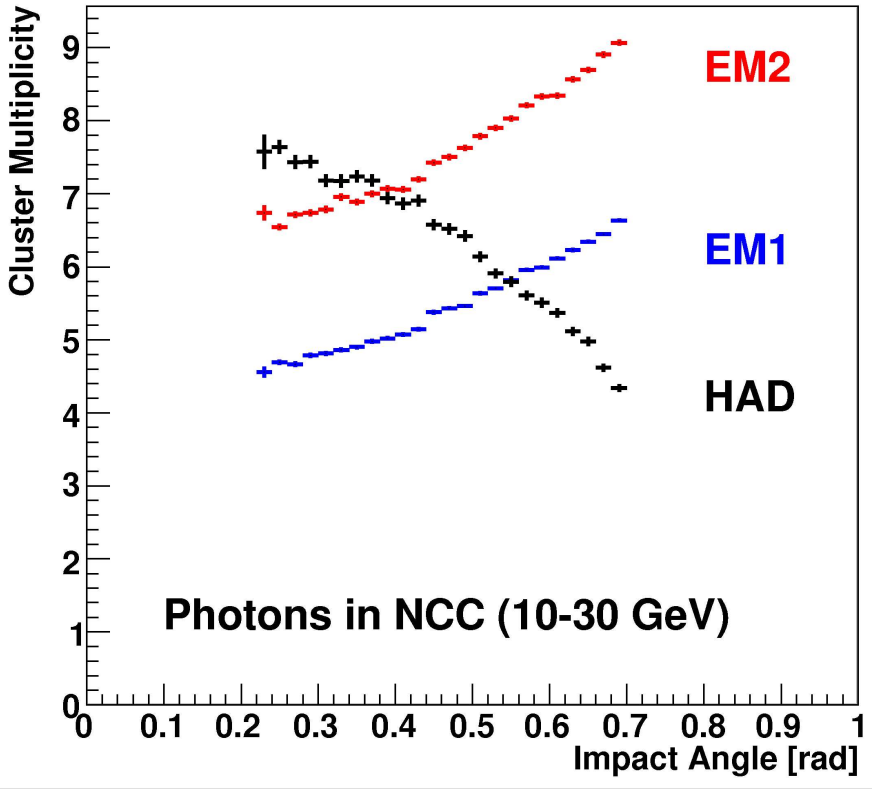

Figure 2.3: Angular dependence of the tower cluster multiplicity in three NCC segments.

but electromagnetic showers in the hadronic segment are totally extinct by the third readout layer. Consequently, the increased aspect ratio of the hadronic segment has no deleterious effect on tracking electromagnetic particles. Fig. 2.3 shows, for each of the three calorimeter segments, how the number of towers that contribute to a cluster depends on impact angle. The tower cluster multiplicity per track rises by less than 50 % between mimimum and maximum impact angles (compared to $\times 2$ increase in the central arm calorimeter). The density of particles hitting the detector decreases towards larger impact angles (smaller rapidities), which minimizes the effect of increased cluster multiplicities on the calorimeter occupancy.

It is indicative to compare the occupancy in the NCC to that in the central arm calorimeters, which are constructed of readout towers with a $45\times45\,\mathrm{mm}^2$ cross-section and an aspect ratio of $\sim$10. An occupancy of 15% in the PHENIX central calorimeters is typical in the most central Au+Au collisions at RHIC energies. Under similar running conditions the occupancy reaches 40% in the NCC (with an energy threshold of 300 MeV), but it becomes comparable to that of the central arm (and comfortable for individual shower reconstruction at least up to rapidities $\sim$ 2) when the energy threshold in the peaking tower is further increased to 500 MeV (see following sections).

Segmenting the NCC longitudinally has a dramatic effect on its performance as a particle identification detector, allowing it to effectively reject hadronic showers by comparing the

measured longitudinal shower development to the parameterized electromagnetic shower shape.

2.2 Simulation

The detector has been modeled in the GEANT-3 based PISA simulation framework ("PHENIX Integrated Simulation Application") which ensured a realistic description of the rest of the PHENIX detector, including all background and albedo sources. A new beam pipe and the Forward Vertex detector (FVTX), planned to be in front of the NCC, have also been fully implemented (see Fig. 2.4). As for the NCC, all enclosures, electronics, outer and interleaved support structures were included in order to make the simulations as realistic as possible. In our χ_C studies we used the standard muon tracking software for muon reconstruction. As for reliability, it should be noted that when the central arm of PHENIX became operational, it turned out that background levels, performance of algorithms, *etc.*, which were predicted based upon PISA simulations were remarkably accurate (within 30%). Therefore, we believe the simulation results in this Chapter are also quite realistic.

Simulated single particles were used to establish energy deposit patterns as a function of momentum, rapidity and particle type; the results were used to calibrate the detector and to establish the primary particle identification cuts, which were then revisited when those single particles (optimum case) were embedded into the underlying "real" events (background). The underlying events were generated with HIJING 1.37 which serves as a standard for PHENIX. Samples of 50K events were produced for the following systems and collision centralities at $\sqrt{s_{NN}}$=200 GeV: p+p minimum bias, d+Au minimum bias, d+Au 0-20 % (most central), Au+Au 0-10 % (most central), 10-20 %, 20-30 %, 30-40 %, 40-50 %, 50-60 %, 60-80 %, 80-92 % (most peripheral). For spin studies, 500 GeV center of mass p+p events were produced using PYTHIA which included both the signal and the background.

After processing signal and background files though PISA, events were then subjected to the detector response chain to make a simulated raw data file. These events were then calibrated and reconstructed as mentioned above. Since the CPU time needed to directly simulate the full luminosity of a RHIC II run is prohibitive, we have simulated small data sets and then scaled up the signals to a full run, using the signal to background and efficiency factors found in the simulation chain.

The analysis code will be optimized for performance and speed while the NCC construction is underway. Cuts and calibrations will be retuned, based upon the real observed performance of the detector.

2.3 Energy calibration

The basic readout units of the NCC are the (sub)towers (energy and time information) and the strips (energy). The energy deposited by showering particles inside the individual Si sensitive elements was digitized into ADC counts, assuming a 13 bits equivalent noise free ADC (14 bits) with a 50 GeV dynamic range in every subtower. Digitization contributes

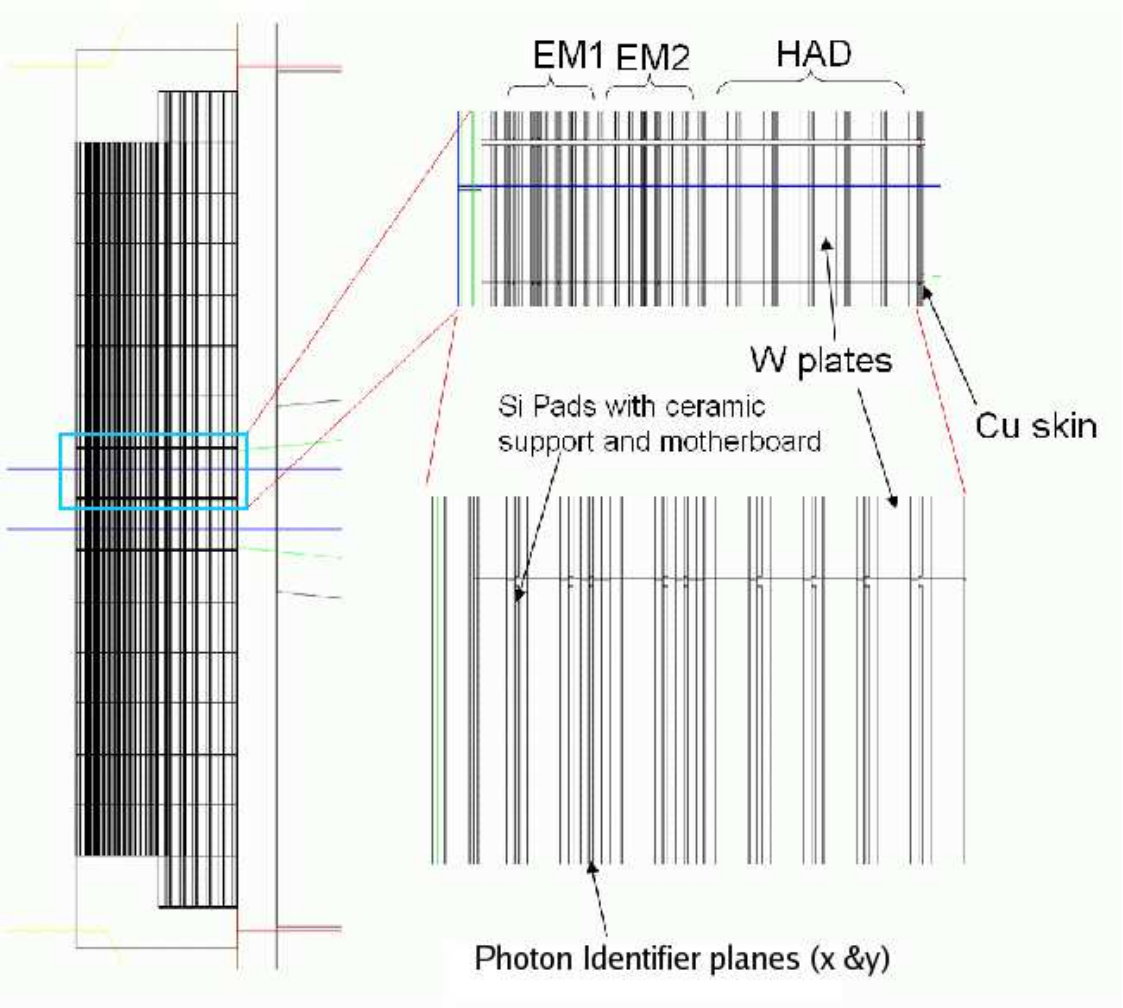

Figure 2.4: GEANT picture showing the implementation of some of the details of the NCC in the simulation.

an energy independent term of ∼50 MeV to the calorimeter energy resolution of $23\%/\sqrt{E} + 1\%E$ [GeV] (at a normal impact). The contribution of the digitization to the NCC energy resolution is shown in Fig. 2.5.

The reverse conversion (ADC counts into measured track energy) was implemented following recommendations for the calibration of longitudinally segmented systems in [13]. Minimum ionization particle losses in individual segments were used to compute relative weights of the segments which we further corrected for the ratio of the total visible energy to the true energy of the impinging photon. This energy calibration procedure was applied directly to the energies seen in the towers and strips. Clustering and track reconstruction were done with energies measured in units of GeV and subject to the precision loss due to digitization.

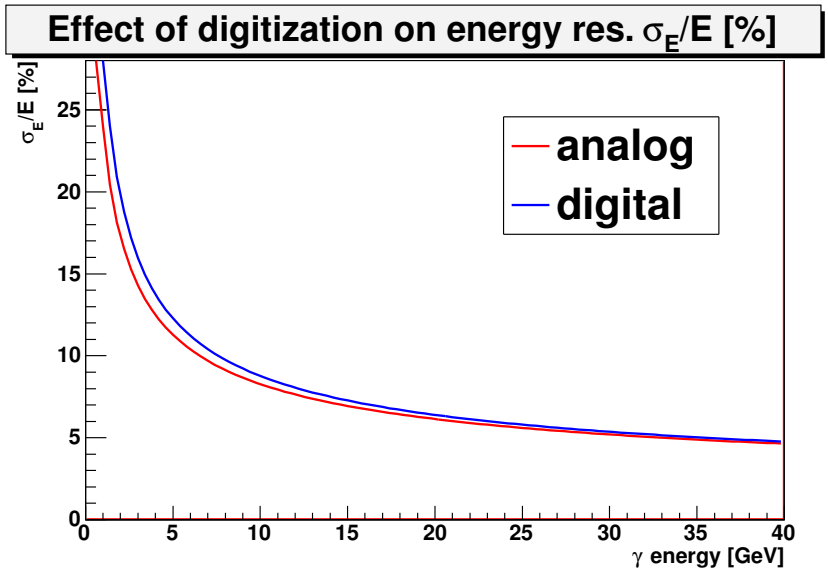

Figure 2.5: Photon energy resolution with and without digitization

2.4 NCC occupancy

Fig. 2.3 shows that the number of hit towers per cluster (corresponding to a single photon of energy between 10 and 30 GeV) as a function of the impact angle for EM1, EM2, and HAD is less than 10. Since each NCC layer (e.g. EM1) has about 2500 channels, the majority of which at rapidities between 1 and 2, the NCC will have reasonable occupancies of <50 % for mid-central Au+Au events.

The occupancy of the NCC in central Au+Au collisions is very high (see Fig. 2.6). However, much of it is due to low energy showers and minimum ionizing particles (MIPs). Low energy showers below about 2 GeV are particularly important for the detection of low momentum "two-track" π^0s (those detected by reconstructing the two photon invariant mass) and the χ_C. After a cut of 300 MeV on the sub-tower energy, the occupancy in the $1 < \eta < 1.5$ region is less than 40 %. At higher rapidities the average energy deposited is higher but a 500 MeV threshold will still allow measurements for two-track π^0s and χ_Cs up to η =2. Direct photons and high p_T "single-track" π^0s (those detected as single showers in the NCC and whose invariant mass is reconstructed using the opening angle and energy asymmetry in the strip detectors – see section 3.3.2) are much less affected. Since these deposit larger energies, they will appear clearly above the background of overlapping low energy showers. We will show in this document that we can measure single track π^0s and photons to at least η =2.5. At higher pseudorapidities a special energy calibration is necessary, as the showers are not fully contained in the NCC. While we believe that ultimately we will be able to make measurements up to η =3, proving it is beyond the scope of the study described in this document.

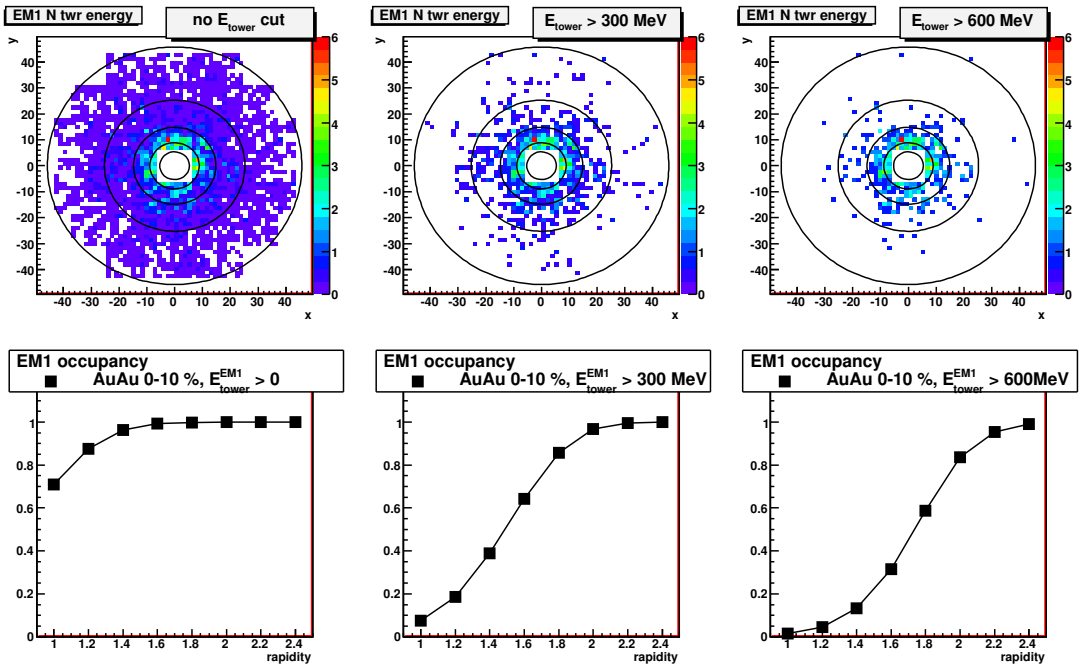

Figure 2.6: Upper row: energy [GeV] deposited in the sub-towers of the NCC EM1 section for a central (0–10 %) Au+Au event, with no threshold (left), 300 and 600 MeV thresholds (middle and right). Colors indicate the total energy deposited in each sub-tower. The energy for a MIP is about 200 MeV. The circles on the plot indicate pseudorapidity in steps of 0.5 with the outermost solid circle showing $\eta = 1$, the next line indicating $\eta = 1.5$, etc. up to $\eta = 3$ for the smallest circle. The bottom plots show the occupancy as a function of pseudorapidity for no cut on tower energy (left), a 300 MeV cut on the tower energy (middle) and a 600 MeV cut (right). For $\eta < 1.5$ and a cut of 300 MeV, the occupancy is below 50 %.

2.5 Cluster and track reconstruction

Clusters are defined as contiguous sets of towers (in a particular layer of the NCC) that *presumably* are part of a shower resulting from the same particle, with an energy and a position assigned to them. Each calorimeter segment is treated independently, thus allowing for a nearly-independent measurement of a weighted center-of-gravity of a shower, in a segment with a typical resolution of ∼0.8 mm. A similar treatment applied to the data collected in the PI layers results in two additional space points associated with the same shower (and a resolution of ∼0.2 mm).

Regression lines through the primary vertex and five points measured inside the NCC (three pad-structured segments and two photon identifier layers) are designated as tracks. Due to the high occupancy, we introduced a flexible algorithm in which lower level objects can ultimately contribute to more than one higher level object (a tower to more than one cluster, a cluster to more than one track). The final energy of the cluster is the sum of the contributions from its individual towers (shared between all clusters which each tower is a

part of). Similarly, the energy of the track is equal to the sum of the calibrated energies of contributing clusters.

In what follows, reconstructed tracks are used for comparing to the particles simulated by event generators and later processed through the whole PHENIX simulation chain (PISA).

2.6 Tracking performance

The details of the NCC tracking efficiency were studied using GEANT simulation data only and will be further improved when test beam data is available. Electromagnetic particles (photons, electrons and π^0s) with transverse momenta between 1 and 20 GeV/c were embedded into background events generated with HIJING. Each event was reconstructed and the original embedded track was found.

Figs. 2.7 a) and b) show the efficiency for finding and identifying electromagnetic showers between 1 and 20 GeV/c in p+p collisions and d+Au collisions. Figs. 2.7 c) though f) show the efficiency for finding and identifying electromagnetic showers in mid-central and central Au+Au collisions. There is a drop-off in efficiency at higher rapidities where the occupancy is high, resulting from a χ^2 cut intended to remove hadrons, but that will also remove any photons that have an overlapping hadron shower. This cut reduces the reconstruction efficiency at high multiplicity. Figure 2.8 shows the energy dependence of the reconstruction efficiency.

Each track reconstructed in the NCC combines points in the calorimeter segments (corresponding to the clusters' centers of gravity), in the PI layers, and the primary vertex. The angular dependence of the position resolution for the calorimeter segments is shown in Fig. 2.9. Clusters in the EM segments are typically spread around the hit vector with rms ∼0.6 cm, nearly independent of the initial particle energy. Tracks with large impact angles have a slightly degraded position resolution in the pad-structured segments of NCC, while measurements in the strip detectors PI1 and PI2 will be affected only slightly by the impact angles. A straight line fit (orthogonal regression) through the points in the calorimeter segments, photon identifier layers and primary vertex, results in an estimate of ∼2.5 mm for the impact position resolution on the front face of calorimeter and of ∼6 mrad for the angular resolution.

Tracking also allows for the calorimeter to point towards the source of the hit particle and thus reduce the background of particles not originating from the collision vertex. The energy dependence of the pointing error, defined as the angle between the hit particle and the straight line fit through all energy weighted points **excluding the primary vertex** is shown in Fig. 2.10. The pointing resolution is driven by the EM2 position resolution (∼6 mm) and the effective track length in the EM section of the calorimeter (∼5 cm). It is close to 0.1 rad for orthogonal impacts and drops to ∼0.18 rad at impact angles close to 45°.

2.7 Identification of electromagnetic tracks

The combination of longitudinal segmentation and lateral towers allows us to form a χ^2 estimator of the likelihood that a track is of electromagnetic origin. This estimator is based upon a parametrization of the average energy and its variance in the calorimeter segments (EM1, EM2 and HAD for longitudinal shape analysis) and calorimeter towers (lateral shape analysis) as function of particle energy and impact angle. A simple polynomial parametrization of deposited energies and variances as deduced from simulation was used for this purpose.

Fig. 2.11 illustrates the hadron rejection in the NCC. By default, the energy spectra of hadrons measured in a shallow calorimeter, which records on average $\sim$50 % of the impinging hadronic energy, is shifted towards lower energies. This downscaling of the energy can be used for direct rejection of candidates in the NCC, helping to substantially reduce the hadronic background to high energy electromagnetic candidates. The remaining high energy hadronic background can be almost entirely removed by analyzing the shower shape (longitudinal and lateral). A suppression factor of 10^{-2} was determined for hadrons with momenta above

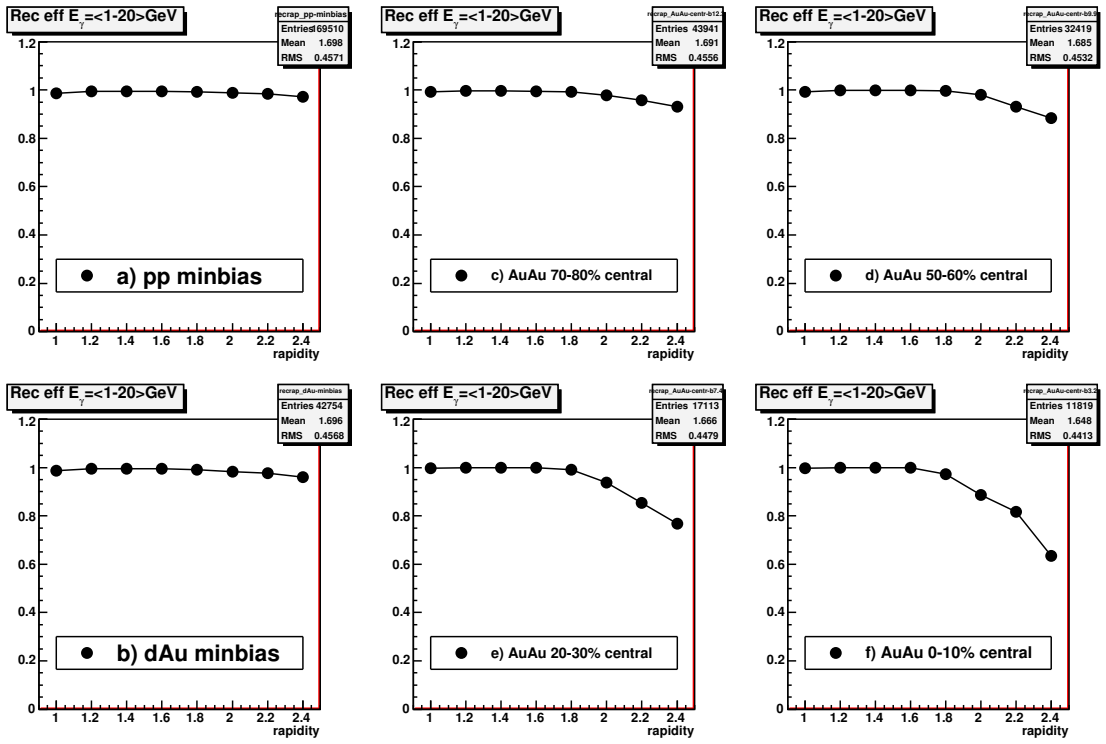

Figure 2.7: Track finding efficiency for photons in the 1-20 GeV energy range vs rapidity in several types of collisions. These efficiencies were computed by embedding photons in background events (HIJING), running though the full GEANT simulation and applying the reconstruction software to the output. Particles which hit the NCC at rapidities higher than 2.5 enter the detector through the beampipe hole (instead of the front face of the detector), and are rejected by the current reconstruction software.

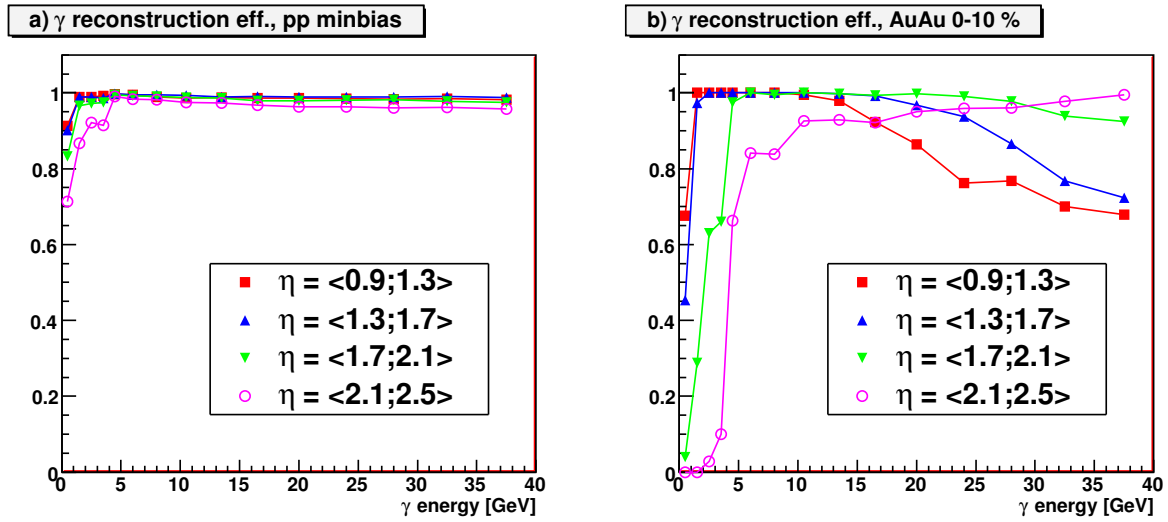

Figure 2.8: Reconstruction efficiency for showers at various energies and rapidities in central 10 % Au+Au collisions.

5 GeV/c, resulting in a few % contribution to the measured cross section for π^0s in the same momentum range. Further reduction of the hadronic background will be provided by matching NCC tracks to charged tracks reconstructed in the PHENIX FVTX.

The currently implemented algorithms are based upon simulation data only. In the future, detailed test beam data will be used to form a better model of the electromagnetic showers, including a good knowledge of correlations so that the proper covariance matrix can be formed and a better χ^2 estimator computed.

2.8 High energy photons

A comparison between simulated (blue) and reconstructed photons (passing identification tests, red) is presented in Fig. 2.12. Both real electromagnetic showers and misidentified showers of hadronic nature contribute to the spectrum of reconstructed photons. In all cases the reconstructed event had one photon embedded into it. The photon energies were uniformly distributed between 0 and 60 GeV, and the population was uniformly distributed in $cos(\theta)$ so that the large impact angles were enhanced. The simulated and reconstructed photon spectra agree well in the peripheral events. As the multiplicity of the underlying event grows, the probability of overlaps increases, distorting the energy resolution and pushing reconstructed spectra towards larger transverse momenta (a well known effect of finite detector resolution leading to the hardening of fast falling spectra). In peripheral events the "efficiency" stays close to 1 at all but the lowest p_T; in mid-central and most central Au+Au events it is reasonable above p_T >5 GeV/c and p_T >10 GeV/c, respectively. This is a problem primarily at high rapidities. For any analysis requiring low energy photons in high multiplicity events, we will limit the η range to between 1 and 1.5 where the occupancy is much lower (Fig. 2.6).

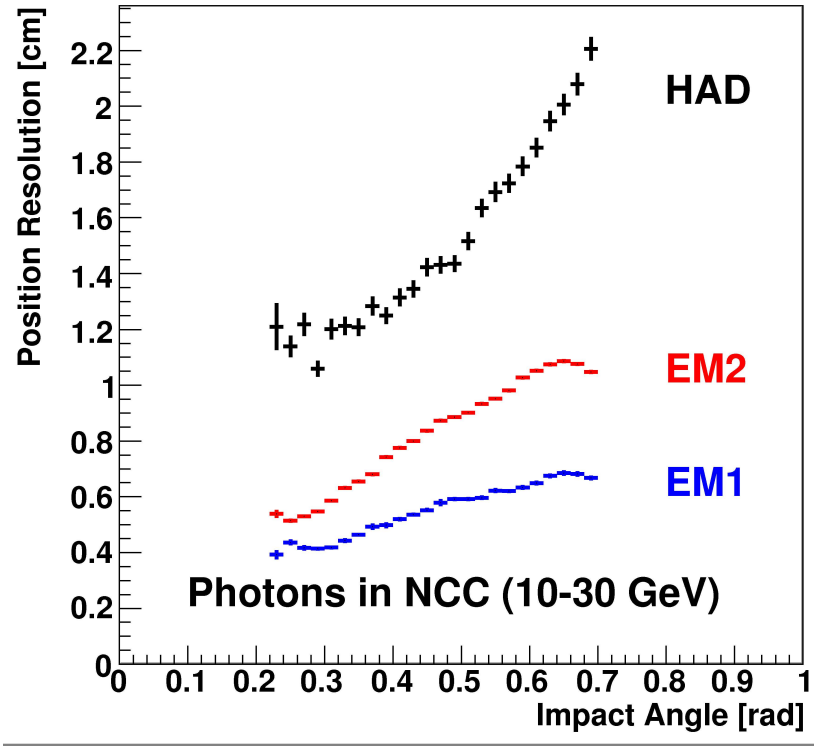

Figure 2.9: Angular dependence of the position resolution in the three NCC segments.

2.9 π^0s

The ability of the NCC to resolve two close tracks in the pad-structured segments is intrinsically limited by the single tower size to ∼40 mr, which is close to the minimum opening angle of two photons resulting from a 5 GeV/c π^0 decay. Below this momentum the decay photons will form two distinct tracks, and π^0s can be reconstructed the traditional way, calculating an invariant mass from each pair of photon candidates within an event and estimating the combinatorial background using event mixing. Low p_T two-track π^0s were generated using the HIJING event generator. For higher p_T we embedded simulated single π^0s into HIJING events. In each centrality bin 1,000 events were generated and reconstructed.

Single photons were selected by requiring tracks with a longitudinal χ^2 <2 and a transverse χ^2 <4 as defined for the calorimetric segments. Fig. 2.13 shows the two photon invariant mass for a variety of centralities from p+p to central Au+Au, and in different p_T and rapidity ranges. Note that the p_T where the two-track method is no longer applicable depends on the rapidity. At $1.0 < \eta < 1.5$, p_T =3.5 GeV/c corresponds to π^0 energies of 6-9 GeV; for $1.5 < \eta < 2.0$, p_T =2 GeV/c corresponds to energies of 4-7 GeV. Since at an energy of ∼5 GeV the two photons begin to merge, we plan to measure two-track π^0s only in the $1.0 < \eta < 2$ region for p+p and d+Au events and $1.0 < \eta < 1.5$ in Au+Au events.

As discussed in the previous section, showers from π^0 decay photons begin to overlap above a π^0 energy of ∼ 5 GeV. In this case the π^0 appears as a single track and is no longer identifiable by traditional methods. We wanted to extend π^0 identification to much higher

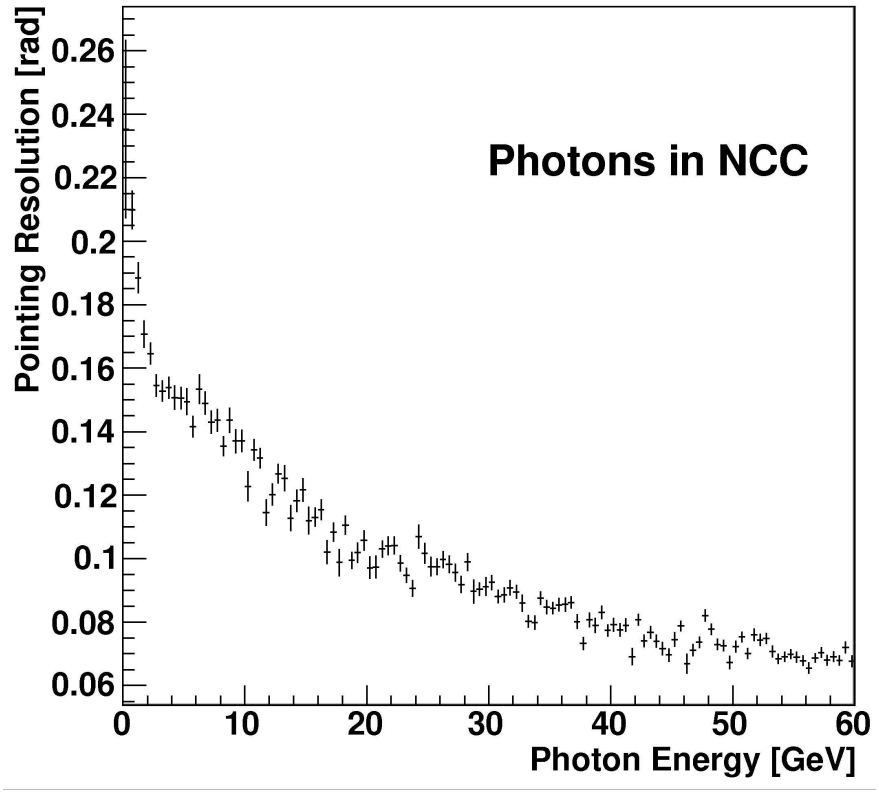

Figure 2.10: Energy dependence of the NCC pointing resolution.

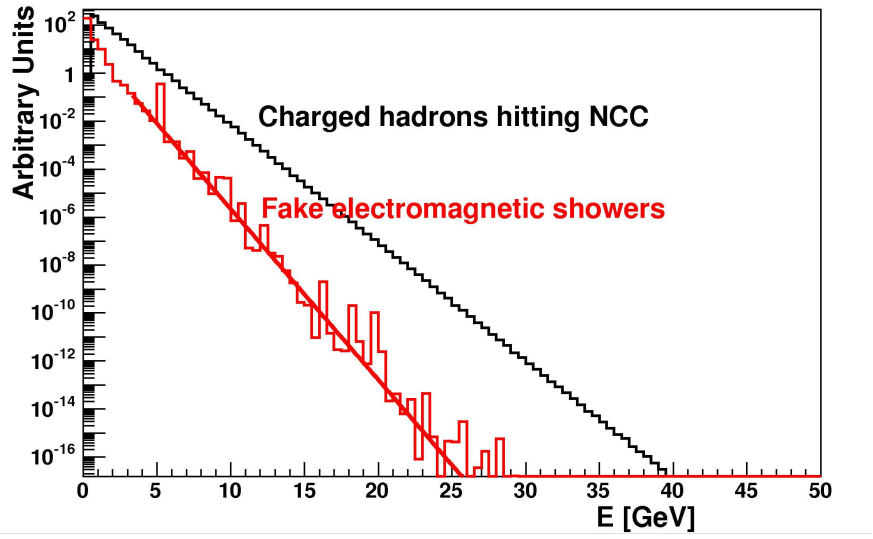

Figure 2.11: Black: Momentum distribution of all hadrons impinging on the NCC at 200 GeV collision energy; Red: energy distribution of NCC tracks that are associated with hadrons and misidentified as electromagnetic showers.

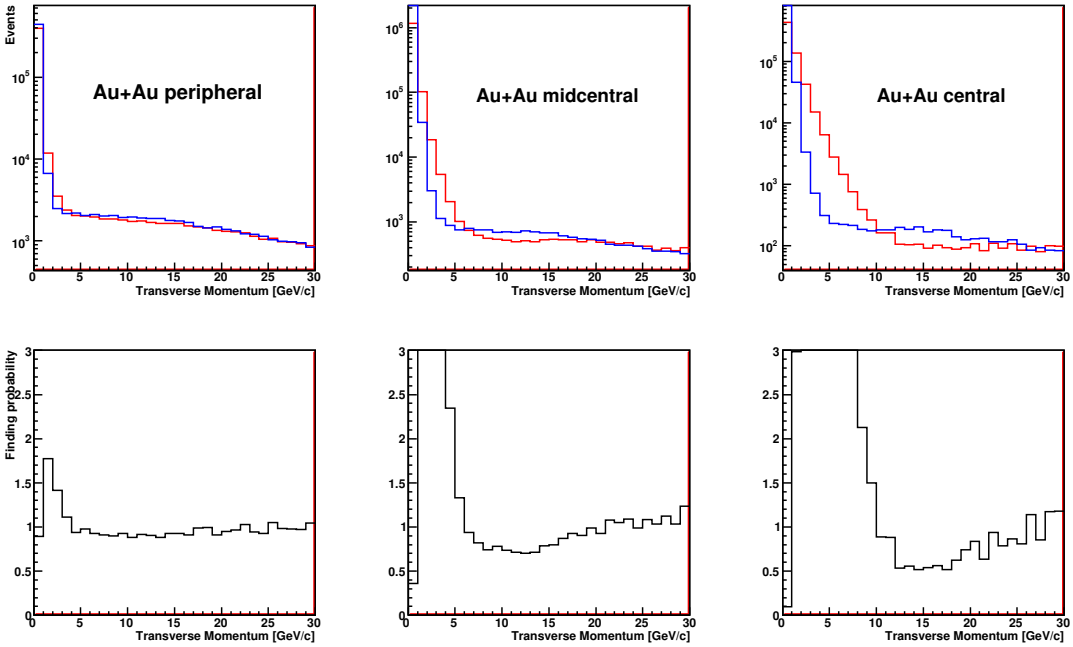

Figure 2.12: Comparison between simulated and reconstructed spectra of photons in the NCC, for events of varying centrality. Top panels - simulated photon spectra (blue) compared to reconstructed (red) spectra of electromagnetic tracks, bottom - ratio of the spectra.

p_T, in part because of the inherent interest in high transverse momentum π^0s but also to reduce the background to the direct photon measurement. To achieve this the calorimeter is supplemented with two high resolution 2-dimensional (X and Y) position sensitive detector layers built of $0.5\times60\,\mathrm{mm}^2$ Si strips, PI1 and PI2. If placed at appropriate depth, these detectors can measure whether the shower is produced by one or two photons. Typically such detectors are placed at $\sim$2 radiation lengths (X_0) and/or at the depth of the shower maximum. However, very extensive simulations have shown that in this configuration the picture in the second layer is totally dominated by fluctuations in the shower development and adds no information to the one extracted from the first layer. Further studies have shown that the best results concerning the efficiency of photon identification and counting are achieved by positioning both layers at a depth range of 2-3 X_0.

In this analysis, each electromagnetic track with energy above 5 GeV is treated as a π^0 candidate. Strips which could be related to the track are identified and considered a "region of interest", within which we search for strip clusters separated by more than two strips. The two most energetic clusters are taken as candidate overlapping photons. Due to fluctuations, the probability of finding at least two such clusters in the region of interest is high, even in the case of tracks originating from a single electromagnetic particle. Hence, the cluster to cluster separation (independently measured in X and Y directions in both 2-D layers), is further used to compute the spatial separation and opening angle, ψ, for the candidate π^0. Using the decay asymmetry, α, of the average of the ratio of ordered cluster amplitudes in

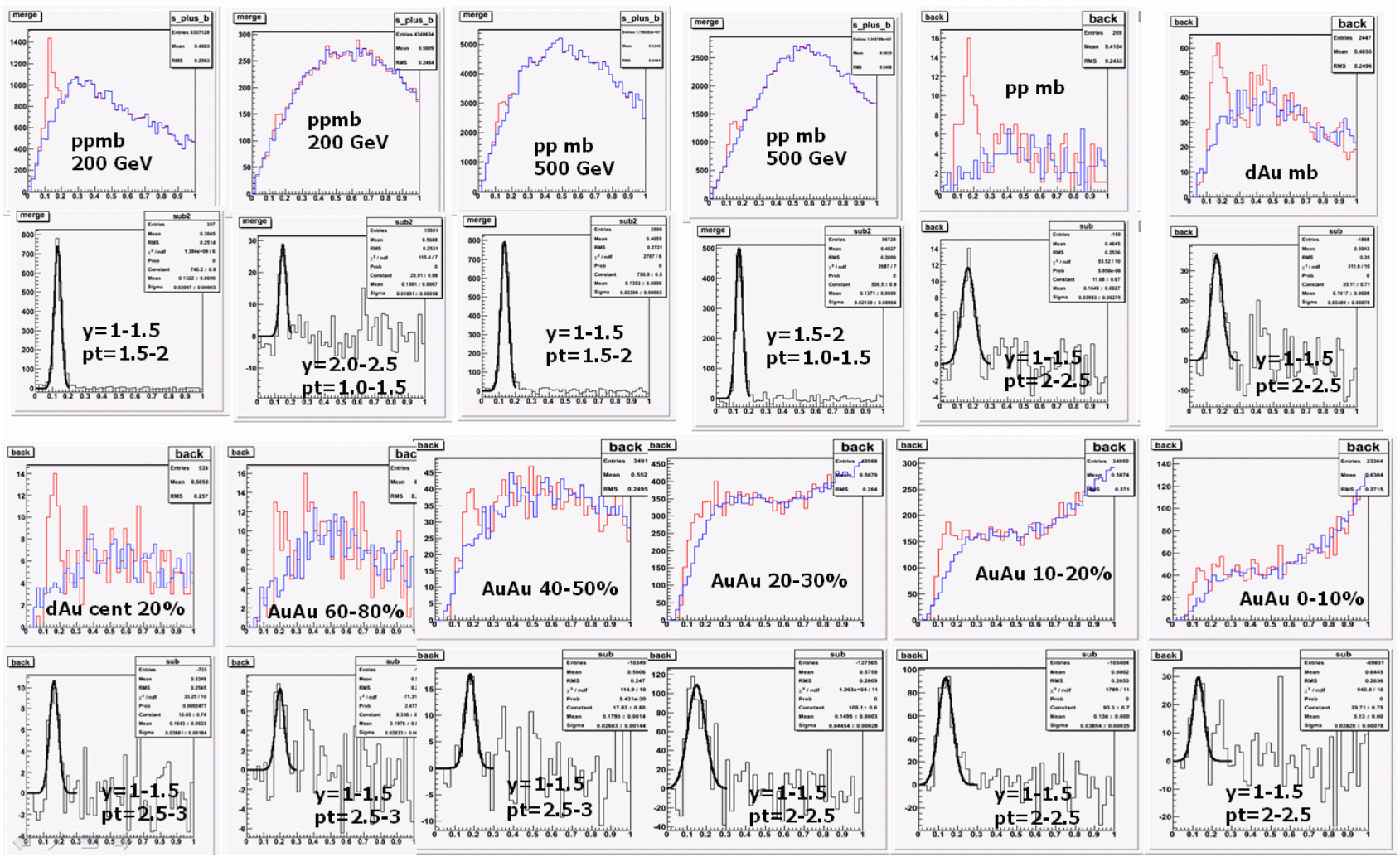

Figure 2.13: π^0 two-track invariant mass for various centrality bins. The first and third rows show the signal (red) and combinatorial background (blue), the second and fourth rows show the subtracted signal.

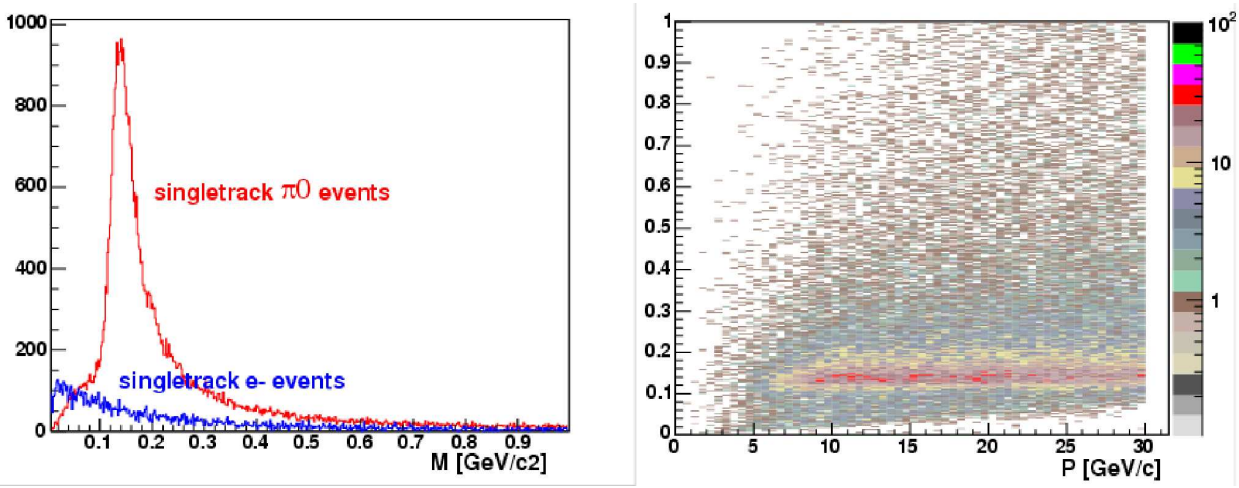

Figure 2.14: Distribution of reconstructed masses for π^0 and electron tracks in the energy range 5-30 GeV that were embedded into p+p events in the NCC. Red: tracks due to overlapping photons from single π^0s; blue: tracks due to single electrons. Right panel: reconstructed masses for π^0 tracks of different energies.

both layers and both (X and Y) directions, one can calculate a mass, m, for the single track electromagnetic shower (Fig. 2.14):

$$m(\psi, \alpha, e_T) = e_T \sqrt{(1-\alpha^2)(1-\cos(\psi))/2}, \tag{2.1}$$

where e_T is the total energy of the pair.

Applying a mass cut of two standard deviations around the π^0 peak to the "single-track" π^0 events retains ∼50 % of the embedded statistics. When similar cuts are applied to the effective mass distributions (after background subtraction) for two-photon pairs in p+p events (Fig. 2.13), the corresponding reconstruction efficiency varies between 90 % around 2 GeV and 5 % at 10 GeV (blue line in Fig. 2.15). The resulting total efficiency for π^0 reconstruction using a combination of the two methods (black line in Fig. 2.15) varies between 90 % in the low energy limit and 40 % at the high energy limit of 30 GeV set by the top RHIC-II luminosity.

Similar efficiency estimates for different event centralities and kinematic ranges were used to establish the statistical sensitivity and estimate the systematic uncertainties assigned to the reconstructed π^0 and direct photon signals used to predict the physics performance of the NCC in the next chapter.

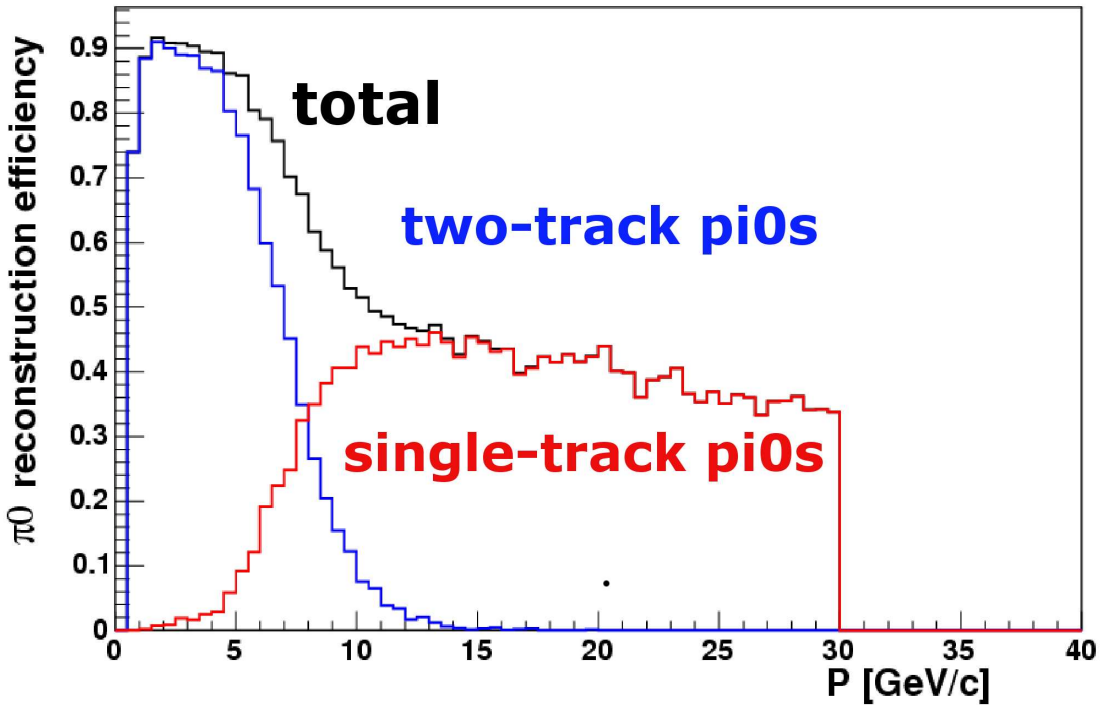

Figure 2.15: Combined reconstruction efficiency for π^0s embedded into p+p events. Blue: mixed background subtraction from two photon effective mass distributions; red: mass assignment to single electromagnetic tracks with multiple clusters in PI layers; black: total efficiency.

Chapter 3

Physics measurements

3.1 Physics signatures and backgrounds

We illustrate the capabilities of the NCC through a full simulation of the following physics signatures

- π^0 yield suppression in hot nuclear matter, direct photon extraction and gluon PDF measurements through γ-jet final states. A two-photon mixed background subtraction technique is used to extract the π^0 signal for p_T <4 GeV/c. The single-track photon deconvolution and mass attribution technique is used at higher p_Ts.

- Nuclear modification factor, R_{AA}, for the χ_C.

We begin by first describing some of the scientific questions which motivate these measurements.

3.1.1 π^0 Suppression and jet measurements

The energy loss of quarks and gluons in the sQGP is of critical importance in the identification of its characteristics. Based upon the suppression of high p_T π^0s at midrapidity, PHENIX has recently published the first quantitative constraints on the opacity parameters [12, 14] of the sQGP – for instance the transport coefficient $\langle\hat{q}\rangle$ estimated within the framework of the Parton Quenching Model. The improved precision of the data allows new questions to be answered. The π^0 suppression at $y = 0$ is apparently constant up to $p_T = 20$ GeV/c (instead of exhibiting a slow, logarithmic rise predicted by ionization-type energy loss models), consistent with a Bremsstrahlung-type, constant fraction $\Delta p_T/p_T$ energy loss. Even more surprising, preliminary results on direct photon production in Au+Au indicate that at very high p_T (>15 GeV/c) photons may also be suppressed. Part of this effect (∼15 %) is expected from the so-called "isospin-effect" [15] but the preliminary data do not exclude the possibility that at some very high p_T photon suppression would be equal to that of hadrons, implying substantial in-medium changes to the structure functions. This would be of utmost interest; unfortunately, it appears to happen at and above 15-20 GeV/c,

a region where the measurement in the central arm becomes technically difficult, but would be feasible with the NCC.

In order to improve the quantitative capacity for experiments to compare to various models, it also becomes necessary to have a calibrated probe that pinpoints the initial energy of the emitted parton. The energy loss of heavy quarks, initially predicted to be quite small, may in fact be rather large [16]. Again, as PHENIX seeks to make such measurements with the addition of vertex detectors (VTX, FVTX), it will be important to tag the initial energy of the scattered parton, which requires extracting direct photons and measuring associated hadrons.

The NCC will make possible the following measurements in the area of parton energy loss:

- It will provide a precision measurement of π^0s in the forward rapidity region allowing for a quantitative determination of opacity parameters as a function of rapidity. In the forward region, there will be competing mechanisms of suppression - the suppression of parton energy loss coming from the sQGP, and the suppression due to the modification of the structure functions in the initial state. Careful measurements as a function of transverse momentum, rapidity, and centrality will allow us to separate such effects. A measurement of the π^0 yield in d+Au will also help pin down any modifications in the initial state parton distribution function.

- It will allow the calibration of the outgoing parton, both for light and heavy quarks, by detecting an opposing direct photon. Such events are rare since they are suppressed by a factor of the electromagnetic coupling constant. In addition to giving a broader rapidity reach, the increased acceptance will greatly enhance the rate at which such events are collected.

- It will allow us to extend measurements of the gluon impact on the spin of the proton. The gluon contribution is negligible in the region of x to which experiments have currently been sensitive – i.e. down to $x \sim 10^{-2}$. However the gluons may contribute strongly at lower x. One of the best probes for the gluons is the direct photon production via the gluon Compton scattering diagram, but the latter can not be measured unless the π^0 is measured and understood.

In order to make such measurements, one must first make measure the π^0 spectrum. Using this information, the direct photon spectrum can be extracted. Finally, correlations can be made on a statistical basis between the direct photon signal, and various high momentum particle signatures – for instance – high p_T charged particles measured in the central VTX detector.

3.1.2 χ_C suppression measurements

A second measurement we will present is the result of the simulation for the detection of χ_Cs, in which the χ_C decays to a J/ψ and a photon, with the photon measured in the NCC and the J/ψ measured in the muon spectrometers via its decay to 2 muons. Charmonium

Table 3.1: Luminosity guidance from C-AD for RHIC II. We assume a 50 % duty cycle for RHIC to give a weekly integrated luminosity. We then assume a 12 week run and a 60 % uptime for PHENIX to give a total integrated luminosity. The maximum rate is the interaction rate at peak luminosity.

Species CM Energy	p+p 200 GeV	p+p 500 GeV	p+Au 200 GeV	d+Au 200 GeV	Cu+Cu 200 GeV	Au+Au 200 GeV
lum ($s^{-1}cm^{-2}$)	1×10^{32}	5×10^{32}	2.5×10^{29}	1.9×10^{29}	8×10^{28}	7×10^{27}
interaction rate	4200	21000	320	585	248	47 kHz
lum/wk ($\mathrm{pb}^{-1}\mathrm{wk}^{-1}$)	33	166	0.083	0.062	0.025	0.0025
Int Lum, $\hat{L}$, (pb^{-1})	238	1195	0.6	0.45	0.18	0.018

bound states were initially thought to be sensitive probes of deconfinement, due to screening effects in a gas of quarks and gluons. Recent measurements of J/ψ suppression ([16, 17]) indicate that its suppression is very similar to what has been seen at CERN energy where the energy density is thought to be 2-3 times smaller. The discovery that the sQGP is strongly coupled also is a challenge to this idea since the correlation length is much larger than was originally thought. There are also other processes such as recombination which would tend to enhance the production of charmonium states. It becomes very important to measure states with various binding energies, which would be affected differently by screening effects. The χ_C is such a state, having a disassociation temperature of $1.16\,\mathrm{T}_C$ compared to $2.1\,\mathrm{T}_C$ (in some models) for the J/ψ and is thus weakly bound. If screening effects were responsible for the suppression of charmonium, then the χ_C should be suppressed more strongly. We will describe the measurement of the suppression of the χ_C as a function of centrality.

In order to disentangle various effects – e.g. suppression and coalescence, a detailed study of the suppression pattern of the J/ψ, ψ', and χ_C as a function of the number of participants, transverse momentum, and rapidity will be necessary. The χ_C, because of its lower dissociation temperature (as computed on the lattice [18]) and its influence on the J/ψ measurements because of feeddown, is a critical element to understand this puzzle, and its implications for deconfinement in relativistic heavy ion collisions.

3.2 Luminosity and rates

In order to estimate potential improvements to already existing measurements or kinematic reaches of the new measurements, we computed expected event rates based upon expected luminosities for RHIC-II provided by the BNL Collider-Accelerator Division (C-AD). We then assume a 50 % duty factor for the RHIC machine, and a 60 % up time for the PHENIX detector during a 12 week run to obtain an integrated luminosity, $\hat{L}$ (see table 3.1).

Our experience with RHIC/PHENIX running in the first 5 years of data taking shows that efficiency will further suffer from several typical losses which are listed in table 3.2. The first arises from a vertex cut, which we take to be ± 10 cm from the nominal collision point.

Table 3.2: Efficiency factors added into the rate calculations. In the analysis we typically require that the vertex be within 10 cm of the nominal collision point (a requirement set by the barrel VTX detector), which results in an efficiency of 0.55 for RHIC II. For RHIC I, the beam spread is larger and results in an efficiency of 0.31. For A+A collisions the minimum bias trigger formed by the Beam-Beam counters are essentially 100 % efficient, however in p+p and p+A collisions there is some loss.

Species	p+p 200 GeV	p+p 500 GeV	p+Au	d+Au	Cu+Cu	Au+Au
vertex cut RHIC II	0.55	0.55	0.55	0.55	0.55	0.55
min bias trigger eff	0.75	0.75	0.90	0.90	1.0	1.0
reconstruction eff	0.80	0.80	0.80	0.80	0.80	0.80
total eff factor RHIC II	0.33	0.33	0.40	0.40	0.44	0.44

We assume 55 % efficiency from losses due to the spread of the beam. Secondly, the PHENIX minimum bias trigger uses the Beam-Beam Counters (BBC) located up- and downstream of the collision point. In the high multiplicity environment of heavy ion collisions, this trigger is almost 100 % efficient. However in low multiplicity p+p and p+A collisions, the efficiency drops since in some cases, no particles actually trigger the BBC. Finally we have taken 80 % for the reconstruction efficiency, a conservative estimate from our experience in past years.

Figure 3.1 shows the raw p_T distributions for π^0s in p+p (RHIC II integrated luminosity, $\hat{L}$, of 240 pb^{-1}) compared to 0-10 % central Au+Au events ($\hat{L}$ of 18 nb^{-1}), see table 3.1. The following data were used as an input to these calculations:

- Inelastic cross section normalized to p+p inelastic cross section at a similar collision energy, σ_{inel}^{norm}, see table 3.3;
- Average number of underlying binary nucleon+nucleon collisions, N_{coll}, see table 3.3;
- (a) NLO pQCD [19] to compute inclusive hard scattering cross section in p+p in the pseudorapidity acceptance of the detector, σ_{hard}^{pp}, or (b) PYTHIA to compute the cross section for γ-jet production in p+p ($\sigma_{\gamma-jet}^{pp}$);

	p+Au	d+Au	Cu+Cu	Au+Au
σ_{inel}^{norm}	30.	73.7	78.	148.
N_{coll}	6.	8.5	52.	258.

Table 3.3: Total inelastic cross sections for several reactions at 200 GeV normalized to p+p inelastic cross section, σ_{inel}^{norm}, and average number of underlying binary nucleon+nucleon collisions, N_{coll} for various collision systems and energies.

The single-particle rate, N_s was calculated as

$$N_s = \sigma_{hard}^{pp} \hat{L} 2\pi p_T \sigma_{inel}^{norm} N_{coll}. \tag{3.1}$$

The γ–jet rate, here defined as the rate of finding a γ in the central arm and a correlated π^0 in the NCC, has to be additionally corrected for the acceptance for finding both the γ and the π^0 in the PHENIX detector, C_{acc}. It is then calculated as:

$$N_{\gamma-jet} = \sigma_{\gamma-jet}^{pp} \hat{L} \sigma_{inel}^{norm} C_{acc} N_{coll} \tag{3.2}$$

The γ–jet acceptance, C_{acc}, is estimated using PYTHIA and tabulated in table 3.4 for various values for the p_T of the direct photon. Table 3.4 summarizes how many γ–jet events to expect in the NCC as a function of the direct photon p_T (any π^0 p_T) given in a 12-week $p+p$ run with RHIC II luminosity.

Table 3.4: γ–jet acceptance factors, C_{acc}, and number of γ–jet events measured in the NCC (with γ in the central arm) for various p_T ranges of the direct photon, in GeV/c, at $\sqrt{s}$ =500 GeV.

$p_T(\gamma)$	5–10	10–15	20–100
C_{acc} $[10^{-5}]$	76	423	1394
$N_{\gamma-jet}$ $[10^3]$	500	200	40

We also include in this plot the rate estimates for direct photons and π^0s in central Au+Au events. The latter data also account for the high p_T suppression of π^0 as measured in the central arm.

Statistically, PHENIX upgraded with the NCC can extend its transverse momentum reach for π^0 and direct photon measurements towards the $\sim$30 GeV/c limit set by expected yields in a 12-week long running period in the RHIC II era.

3.3 Physics with neutral pions

A number of physics signals rely on π^0 measurements. For instance, the nuclear modification factor, R_{AA}, of neutral pions at forward rapidity; the gluon distribution function at low-x seen through the measurement of a jet related π^0 at forward rapidity in conjunction with direct photon in the central arm; the measurement of direct photons at forward rapidity, for which the π^0s are a source of background.

State-of-the-art NLO pQCD calculations [20] (see Fig. 3.1) were used to estimate the expected number of direct photons and π^0s in the NCC as well as the rate of direct photon-jet events. Similar estimates accounting for the acceptance effects in correlated γ-jet production (3.4) were also used to study upgrade effectiveness for gluon PDF measurements in the low-x limit (see below).

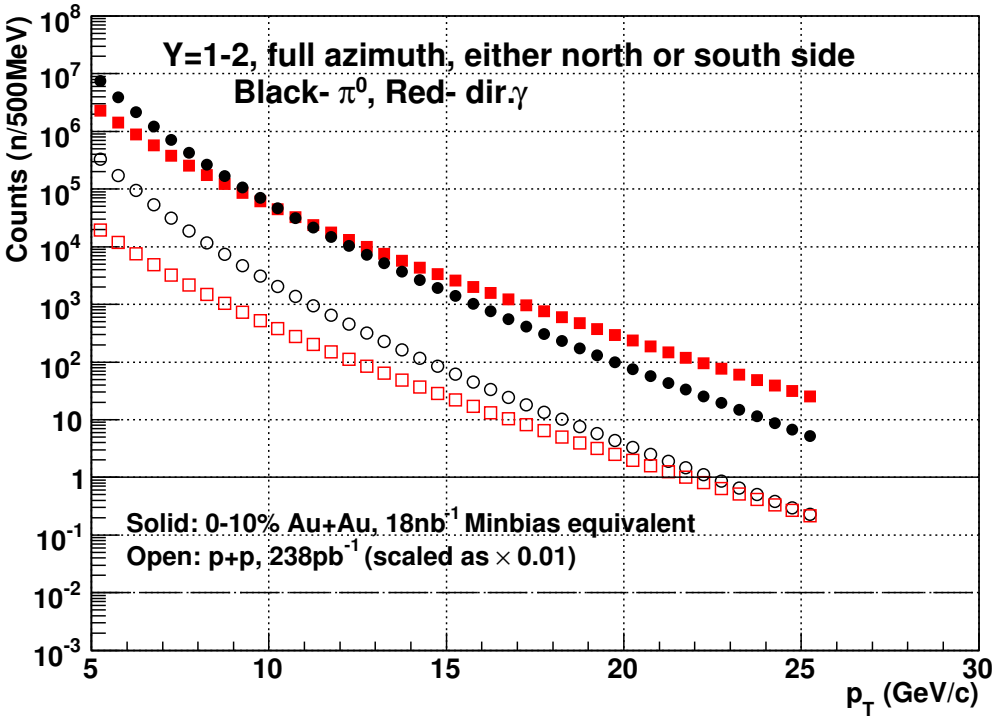

Figure 3.1: Rate estimate for π^0 and direct photons for p+p and Au+Au (0-10 % centrality) collisions at 200 GeV based upon expected RHIC-II integrated luminosity (12 weeks of running). A constant value of $R_{AA} = 0.2$ has been assumed for the case of pi^0s in central Au+Au collisions.

Corrections for losses due to reconstruction inefficiencies (largely overestimated due to deficiencies in the reconstruction algorithms), as discussed in the previous chapter, were used to compute statistical and systematic errors applicable to final physics observables presented in the next sections. The estimates were made for various collision systems (p+p, d+Au, Au+Au) and a range of centralities.

3.3.1 π^0 signal reconstruction in two-photon combinations

The details of the procedure used to reconstruct the π^0 invariant mass distribution are described in Chapter 2. The signal can be clearly seen at all rapidity values (impact angles) in p+p and d+Au data. In high multiplicity central Au+Au events the signal to background drops, so the momentum threshold must be raised for the π^0s to emerge above the background of soft showers due to the non-electromagnetic component of secondary particles in the event. The efficiency of π^0 reconstruction, estimated by counting residual hits left inside the π^0 mass range in the two-photon effective mass distribution after background subtraction, is shown on Fig. 3.2 for minimum bias p+p events.

The losses at low momenta (left panel) reflect acceptance and degraded resolution (low energy photons are strongly affected by the underlying event). The efficiency also drops

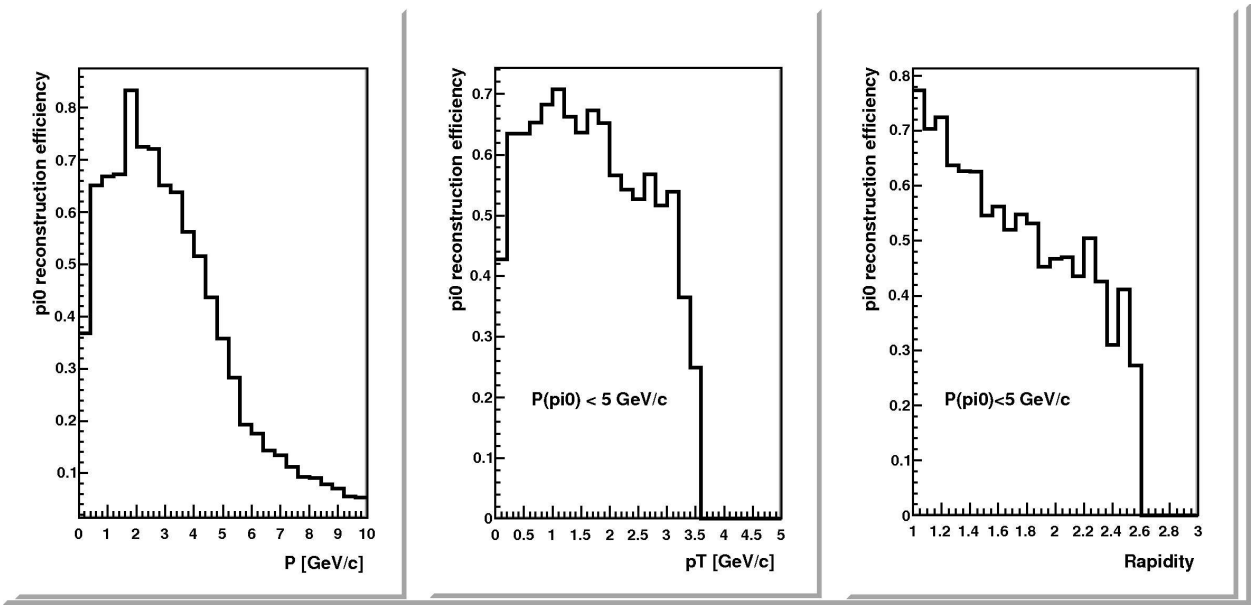

Figure 3.2: Efficiency for finding a π^0 using the two track invariant mass method vs π^0 momentum (left), transverse momentum (center) and rapidity (right).

rapidly at large momenta because the photons from π^0s with energies greater than about 5 GeV begin to merge in the NCC. For π^0s with momenta below 5 GeV/c the efficiency varies little as a function of the transverse momentum which is now geometrically limited to $\sim$3.5 GeV/c and drops towards larger rapidity due to the change in the flight path of photons at different impact angles.

3.3.2 π^0 signal reconstruction in a single-track mode

The technique of reconstructing and identifying single-track π^0s has been described in some detail already, but we will repeat key features here. Fig. 3.3 shows the invariant mass distribution obtained in simulated events consisting of a single thrown π^0. In this case, 10000 π^0s with $12 < p_T < 13$ GeV/c were thrown in the NCC acceptance. Over 90% of those particles were reconstructed as single-track π^0 candidates; that is, as a single set of calorimeter clusters in the NCC satisfying an electromagnetic χ^2 cut and with a separable pair of clusters in each of the PI layers. Of the thrown π^0s, roughly 55% then have an invariant mass that falls within $\pm$40 MeV of the nominal π^0 mass.

The key question, however, is how well one can reconstruct these single-track π^0s in central Au+Au events. And, more to the point, one would like to know how the extraction of physics quantities in central Au+Au depends on the reconstruction of the single-track π^0. There are several quantities needed for this estimate. One is the reconstruction efficiency, the next is the probability for misidentifying a particle as a single-track π^0 (primarily single photons) and the final bit is an estimate of the relative abundance of true single-track π^0's and single photons at the same (y, p_T).

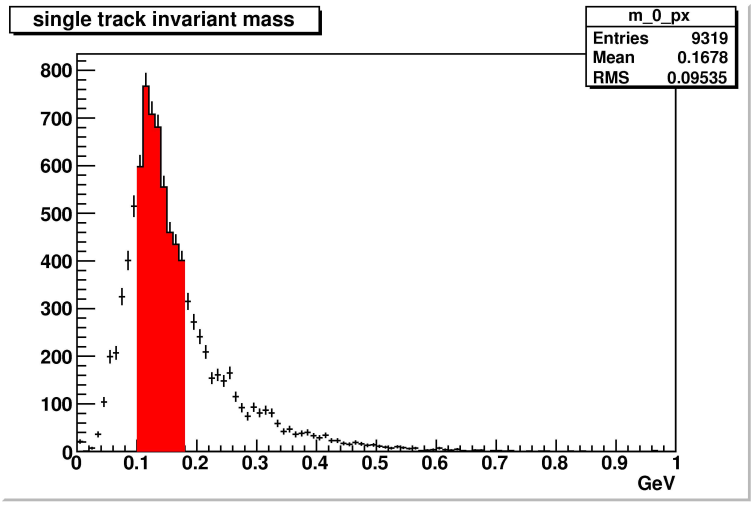

Figure 3.3: Invariant mass of all single-track π^0 candidates in single particle GEANT events.

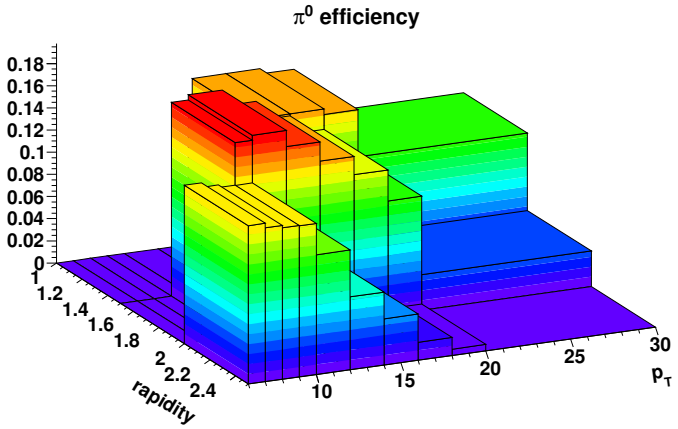

Figure 3.4: Efficiency for reconstructing π^0s in central Au+Au HIJING events as a function of (y, p_T).

We will use here a method of determining the reconstruction and identification efficiency for single-track π^0s that is very similar to that described by WA98 in [21]. We throw a single π^0 and reconstruct it. Then we throw a full central Au+Au HIJING event and reconstruct that. Finally, we mix the single π^0 into the HIJING event and reconstruct that. From this reconstructed mixed event we identify tracks that already appeared in the reconstruction of the plain HIJING event. We search through the remaining tracks to see if the originally thrown π^0 can be found. We obtain the efficiency by dividing the distribution of π^0s in the final instance by the distribution of π^0s reconstructed from single track events. A two-dimensional plot of the reconstruction efficiency in central Au+Au as a function of (y, p_T) is shown in Fig. 3.4. The efficiency peaks at around 20% and falls off with increasing p_T and rapidity. Again, this should be compared to an efficiency of about 55% for a single π^0 not

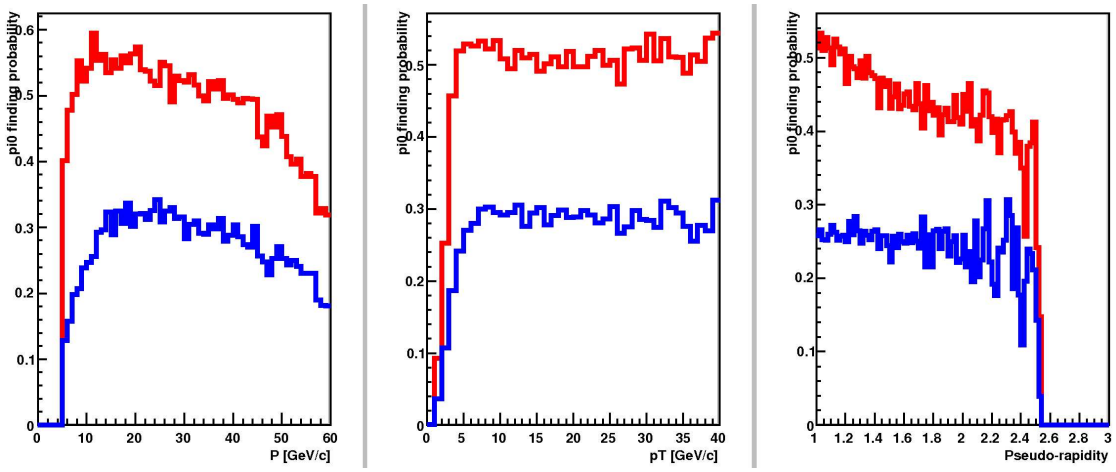

Figure 3.5: Probability of reconstructing a thrown single π^0 as a single-track π^0 (red lines) compared to the same probability for a thrown single photon (blue lines) vs momentum, transverse momentum and pseudorapidity.

embedded in an underlying event as shown in Fig. 3.5. The ratio of photons to π^0s in p+p and d+Au is significantly less than one (O(10^{-2}) at low p_T and rises with increasing p_T [22]. Fig. 3.5 also shows the probability of single photons being misreconstructed as single-track π^0s.

In determining the uncertainty on R_{AA} we need to take into account the relative uncertainties on the π^0 yield in Au+Au and in p+p, which depend on (y,p_T).

3.3.3 π^0 R_{AA}

Low p_T π^0s will be measured with a minimum bias trigger, and in our estimates we assume that both for p+p and Au+Au collisions we can record 10^9 events resulting in γ/π^0 yields close to those shown in Fig. 3.1. For triggered p+p events, the required rejection factor is $\sim 10K$ in order to make use of the entire bandwidth at RHIC-II luminosities – for this the threshold must be set to ~ 8 GeV. For Au+Au the required rejection factor is ~ 30. While the estimates below are based upon central arm (midrapidity) rates, the rejection factors should be similar in the 1.0-1.5 rapidity range.

The signal extracted from the (necessarily limited) number of simulated events has been scaled to full luminosity as follows. For $p_T < 4$ GeV/c HIJING was used directly, therefore, adjustments for cross-section were not needed: the data were simply scaled up to the appropriate luminosity. At higher momenta we embedded single π^0s into "real" events. In order to get the right statistics first we found the appropriate luminosity corresponding to the actual number of embedded particles, then we added the proper number of non-embedded (pure background) events, finally we scaled the resulting plot to RHIC-II luminosity (1B minimum bias events for $p_T < 8$ GeV/c and the full RHIC-II luminosity above that).

Detector effects (resolution, overlaps, misidentification, etc.) distort the measured spectrum. The original π^0 spectrum has been restored as follows (the procedure is similar to the

one used in the central arm). First we chose an approximate spectral shape – in this case a simple power law for the lower centralities and a exponential for the higher centralities, and generate an "input histogram" with it (in a specific slice of rapidity). Next (using the known kinematics) we let the π^0s decay. The resulting photons are smeared with the known resolution function of the detector, acceptance cuts are applied (opening angle, energy, asymmetry) to match the cuts used in the data analysis, and we fill a second, "output histogram" with the reconstructed p_T of the properly reconstructed π^0s. (Note that the rapidity doesn't change appreciably.) The detector response function DRF is then the ratio

$$DRF = \frac{output\ histogram}{input\ histogram}$$

The measured p_T spectrum is then divided by the DRF giving us a initial estimate of the real p_T spectrum. This is then used as input and the whole procedure is repeated until the input and output spectra agree. Fig. 3.6 illustrates the convergence of such unfolding using central arm data: already after the first iteration the differences between the unfolded measured and the true input spectrum are less than 5 %.

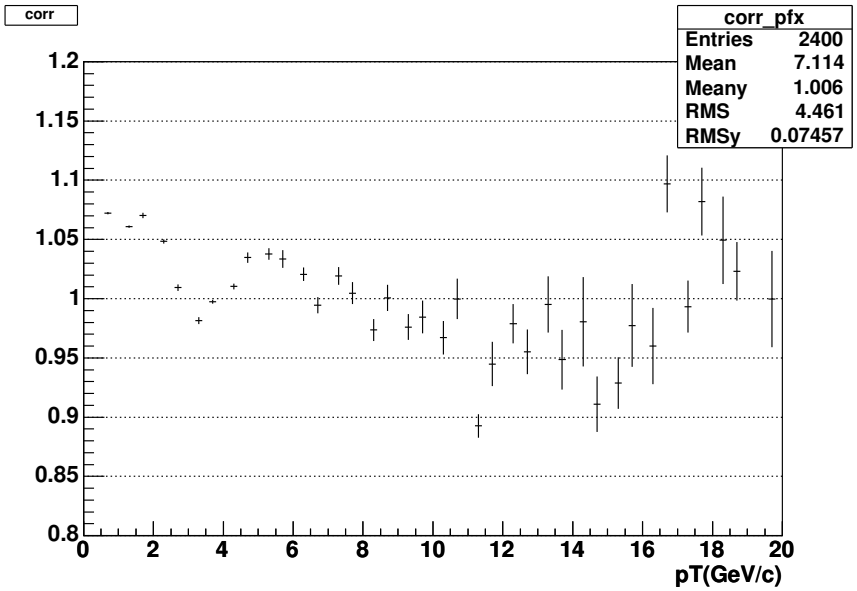

Figure 3.6: Ratio of the unfolded measured spectrum and the true input spectrum after the first iteration. This example (from a central arm analysis) shows how quickly the procedure converges.

We then scale the p+p spectrum by the number of binary collisions in Au+Au and divide by it the corresponding Au+Au spectrum to get the nuclear modification factor R_{AA}, as shown in Fig. 3.3.3 for various centrality values. Note that the error bars are statistical only.

The uncertainty on R_{AA} using the single-track π^0 technique grows with p_T in a manner not so different than that seen in the central arm measurement of R_{AA} using two-track π^0s.

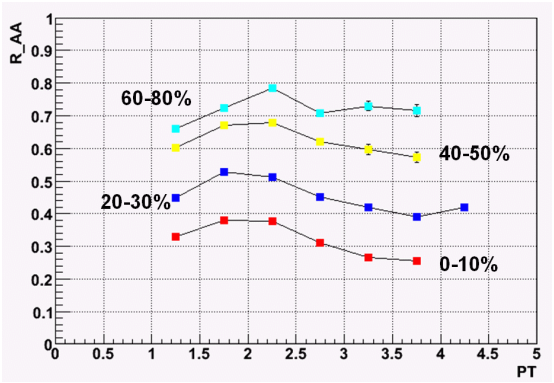

(a) R_{AA} for $\pi^0 \rightarrow \gamma + \gamma$ for various values of centrality. The value of R_{AA} is assumed to be the same as that seen in the central arms, the error bars reflect the precision possible from a one run at RHIC II luminosities. The p_T reached is about 4 GeV. Above this p_T, the single track π^0 takes over.

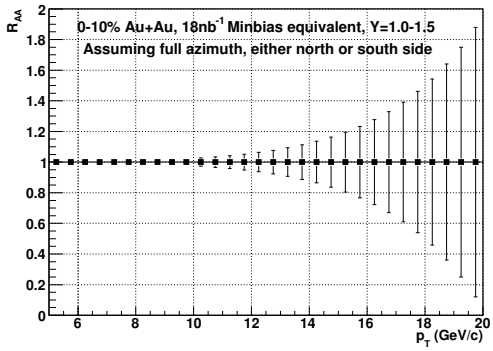

(b) Figure: R_{AA} for "single track" π^0's. The error bars reflect the precision possible in one run at RHIC II luminosities. We assume a suppression pattern similar to that seen in the central arms, hence statistics runs out at ∼15 GeV.

Figure 3.7: Estimates for the uncertainties on the determination of R_{AA} using a two-track reconstruction of the π^0 at relatively low p_T (3.7(a)) and at higher p_T (3.7(b)) using the method of single-track π^0 reconstruction.

At a p_T around 12 GeV/c (a lower p_T than in the central-arm case) the uncertainty rises to 100 %, driven largely by the misidentification of single photons. Up to around 10 GeV/c, though, the uncertainties are small.

3.3.4 π^0 measurements and direct photons

Direct photons are defined as those photons that do not come from final state hadron decays ($\pi^0 \rightarrow \gamma\gamma$, $\eta \rightarrow \gamma\gamma$, *etc.*). In high multiplicity heavy ion collisions, direct photons can only be measured by first establishing the spectra of inclusive photons, then subtracting from it the part attributable to hadron decays (the difference being the direct photon spectrum), which can be simulated once the relevant hadron spectra are known. Due to kinematics, relative hadron yields and branching ratios, the overwhelming part of hadron decay photons at any given p_T comes from π^0, and the figure of merit to judge the feasibility of the direct photon measurement is the (p_T dependent) ratio of the direct photon and π^0 yields. As seen on Fig. 3.1 at and below 5GeV/c the direct photon signal is a few percent in p+p and less than 10-20% in central Au+Au, and probably not measurable. However, above $p_T > 5$GeV/c the S/B rises quickly, particularly in central Au+Au collisions, reaching unity already around $p_T = 10$ GeV/c, largely due to the factor of 5 suppression of π^0 observed at mid-rapidity [12]. Of course this gain in S/B comes at a price of increased occupancy and overlap probability in the NCC from the underlying (central) Au+Au event.

Since the "statistical" procedure described above involves small differences of large num-

bers (inclusive minus hadron decay spectrum), particularly at lower p_T, instead of their spectrum direct photons are often characterized by the "double ratio" or "photon excess ratio", which is defined as

$$R = \frac{\gamma_{inc}/\pi^0_{meas}}{\gamma_{bgd}/\pi^0_{fit}}$$

where γ_{inc} and π^0_{meas} are the measured inclusive photon and π^0 spectra, respectively, γ_{bgd} is the expected photon spectrum from all hadron decays, simulated based upon the hadron measurement, and π^0_{fit} is a fit to the measured π^0 spectrum. R is unity if there are no other photon sources besides hadron decays, and goes above unity in the presence of direct photons. Besides having this clear and straightforward interpretation, another advantage of R is that many of the systematic errors of the photon and π^0 measurements cancel in this ratio, including the crucial error of energy scale (which is usually the largest contributor to the systematic uncertainties in γ and π^0 measurements).

In what follows we consider the rapidity region of $1 < y < 2$, where the single-track γ/π^0 separation is most extensively studied. The calculated reconstruction efficiency for photons of p_T >5 GeV/c is ∼90 %, i.e., 90% of the true, single photons will survive the particle identification cuts. However, the sample obtained will have significant contaminations. A mass cut to remove obvious single-track π^0 candidates reduces the photon efficiency itself to ∼75 % in peripheral, and ∼50 % in the most central events. We assume that this additional (centrality dependent) 15-40 % loss from single photons misidentified as π^0s can be properly estimated by simulations. Conservatively, we assign 10 % error to the photon reconstruction itself and another 10 % to the false rejection of single photons as single-track π^0s. The third most important error is due to the energy scale uncertainty and smearing; based upon our experience in the central arm of PHENIX this error is estimated as 10 % (it should be noted that part of it cancels in the double ratio R). Being uncorrelated, the three contributions listed above give 17 % systematic error. There are, however, a few other contibutors that are smaller (based upon our analyses in the central arm) and are not listed here:

- Hadron contamination to single track π^0 or single photons (this should be negligible for all hadrons except antineutrons, which in turn are suppressed in the forward direction);
- Contributions from particles generated far from the vertex (like $K^0_S \to 2\pi^0 \to 4\gamma$);
- Prompt electrons which we expect to be tagged by the FVTX.

The predicted "double ratios" (calculated as $R - 1$, instead of R) along with their estimated errors are shown on Fig. 3.8. In the shaded areas, current ambiguities in the efficiency determination for π^0 and single inclusive photons are too large; further studies are needed to decide if the measurement is feasible or not.

The direct photon yield can be obtained as:

$$N^{\gamma}_{dir.} = N^{\gamma}_{inc.} \cdot \left(1 - \frac{1}{R}\right) \tag{3.3}$$

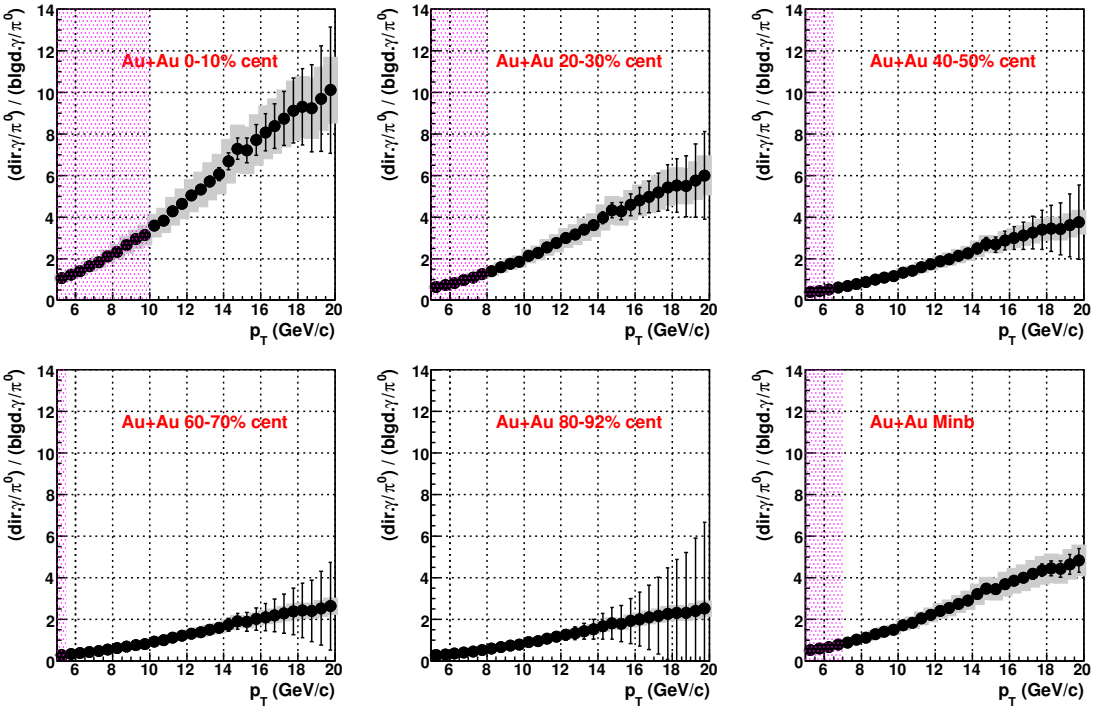

Figure 3.8: Double ratios $(\gamma_{meas}/\pi^0{}_{meas})/(\gamma_{bkgd.}/\pi^0{}_{fit})$ in Au+Au collisions for various centralities, with their estimated errors. In the shaded areas current ambiguities in determining the efficiency are too large.

When the error components are factorized as "$N^{\gamma}_{inc.}$", "N^{π^0}", and "$(N^{\gamma}_{bg.}/N^{\pi^0})_{MC} = N^{MC}$", the error on direct photon can be propagated as follows:

$$
\begin{aligned}
(\delta N^{\gamma}_{dir.})^2 &= (\delta N^{\gamma}_{inc.})^2 \left(\frac{\delta N^{\gamma}_{dir.}}{\delta N^{\gamma}_{inc.}}\right)^2 + (\delta N^{\pi^0})^2 \left(\frac{\delta N^{\gamma}_{dir.}}{\delta N^{\pi^0}}\right)^2 + (\delta N^{MC})^2 \left(\frac{\delta N^{\gamma}_{dir.}}{\delta N^{MC}}\right)^2 && (3.4)\\
&= (\delta N^{\gamma}_{inc.})^2 \left(\left(1 - \frac{1}{R}\right) + N^{\gamma}_{inc.} \cdot \frac{1}{R^2} \cdot \frac{\delta R}{\delta N^{\gamma}_{inc.}}\right)^2 && (3.5)\\
&+ (\delta N^{\pi^0})^2 \left(N^{\gamma}_{inc.} \cdot \frac{1}{R^2} \cdot \frac{\delta R}{\delta N^{\pi^0}}\right)^2 + (\delta N^{MC})^2 \left(N^{\gamma}_{inc.} \cdot \frac{1}{R^2} \cdot \frac{\delta R}{\delta N^{MC}}\right)^2 && (3.6)\\
&= (\delta N^{\gamma}_{inc.})^2 + (\delta N^{\pi^0})^2 (N^{MC})^2 + (\delta N^{MC})^2 (N^{\pi^0})^2 && (3.7)\\
&= (\delta N^{\gamma}_{inc.})^2 + \left(\frac{\delta N^{\pi^0}}{N^{\pi^0}}\right)^2 \left(\frac{N^{\gamma}_{inc.}}{R}\right)^2 + \left(\frac{\delta N^{MC}}{N^{MC}}\right)^2 \left(\frac{N^{\gamma}_{inc.}}{R}\right)^2 . && (3.8)
\end{aligned}
$$

Then,

$$
\left(\frac{\delta N^{\gamma}_{dir.}}{N^{\gamma}_{dir.}}\right)^2 = \left(\frac{R}{R-1}\right)^2 \cdot \left(\frac{\delta N^{\gamma}_{inc.}}{N^{\gamma}_{inc.}}\right)^2 + \left(\frac{1}{R-1}\right)^2 \cdot \left(\left(\frac{\delta N^{\pi^0}}{N^{\pi^0}}\right)^2 + \left(\frac{\delta N^{MC}}{N^{MC}}\right)^2\right) \quad (3.9)
$$

In this case, the systematic error for "MC" is zero, the one for "gamma" is 10 %, and that for "π^0" is 12.2 %. The statistical error is propagated similarly. The resulting direct photon spectra and R_{AA} are shown in Fig. 3.9 and Fig. 3.10, respectively.

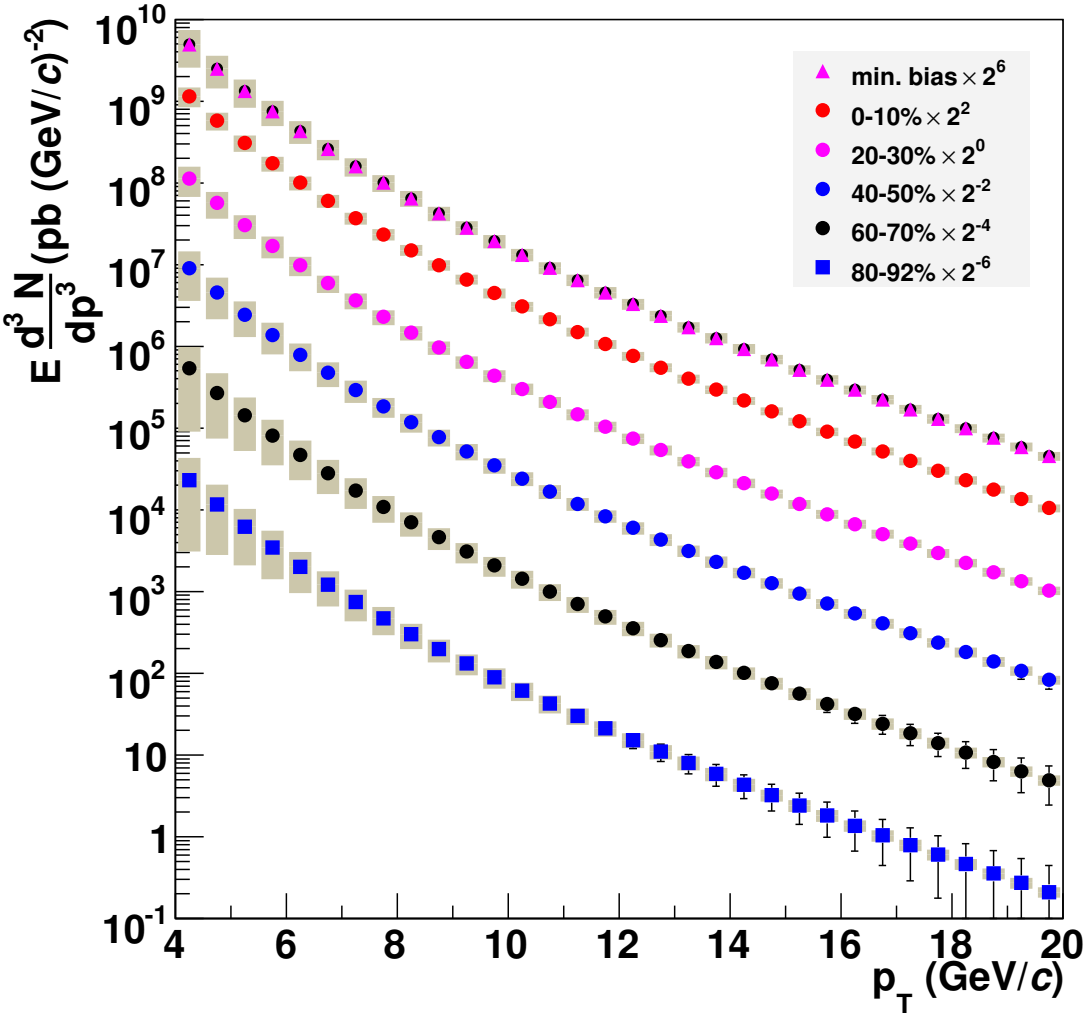

Figure 3.9: Direct photon spectra in Au+Au

3.3.5 π^0 measurements and jet reconstruction

The third segment of the NCC, the HAD segment, increases the calorimeter thickness to 1.3 absorption lengths (L_{abs}) to help with hadron rejection. As a byproduct it also improves the hadronic energy measurement which is particularly crucial for PHENIX's jet reconstruction abilities, since the calorimeter is not fronted by a spectrometer which would allow one to measure the momentum of the charged hadronic fragments. In Fig. 3.11, the PYTHIA jet energy is compared to the total reconstructed energy using a cone algorithm, showing that

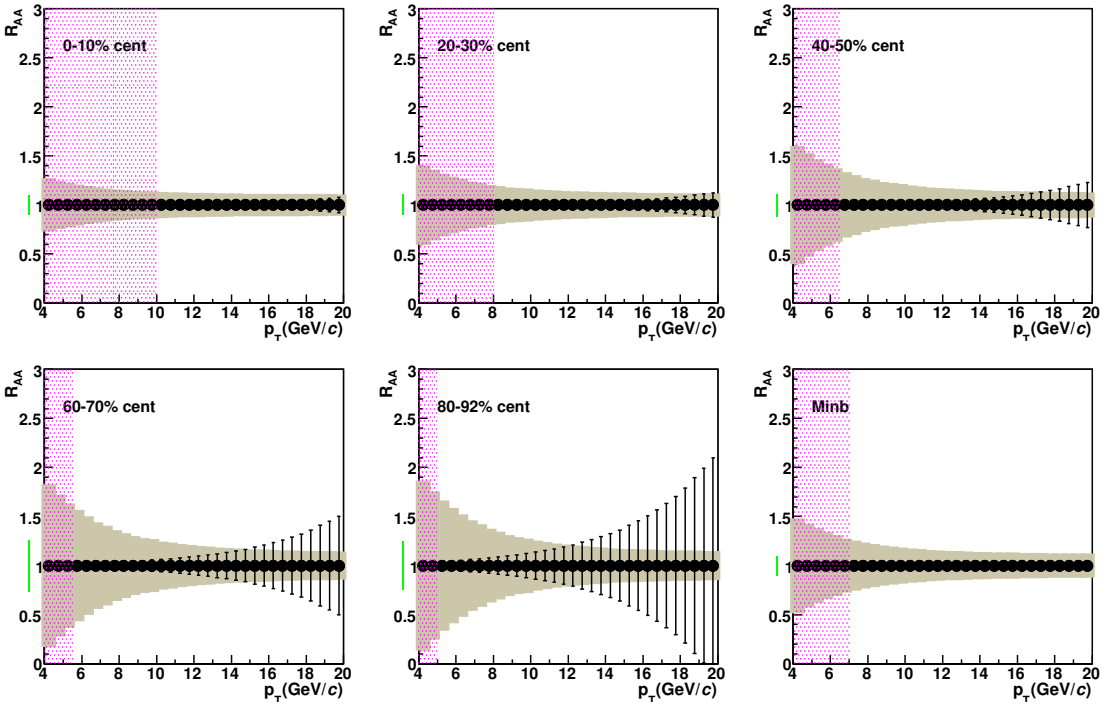

Figure 3.10: Direct photon R_{AA} in Au+Au

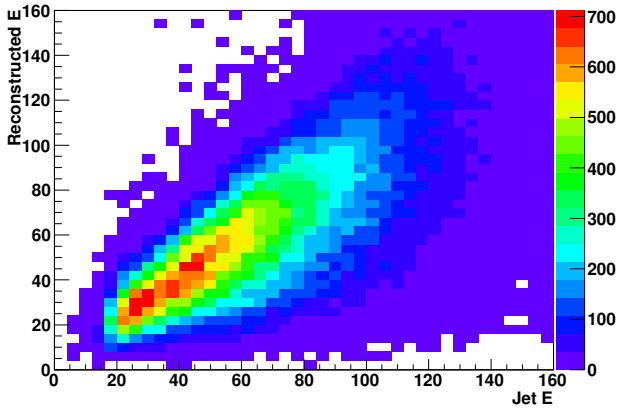

Figure 3.11: Reconstructed jet energy from a cone within $\Delta R < 0.5$ vs the PYTHIA jet energy in GeV

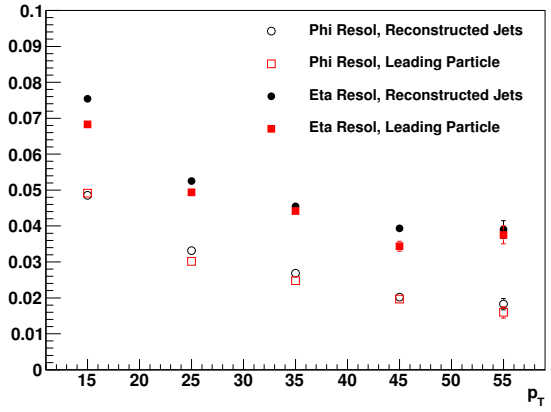

Figure 3.12: Angular resolution of the reconstructed jets and leading particles in azimuthal angle ϕ and pseudorapidity η.

the NCC will make reasonable reconstructions of jets. Further improvements are expected from calibrating the hadron response as well as better reconstruction algorithms, such as those based on a particle flow analysis.

The following relations, based on a leading order analysis, are used to get the kinematic variables: $x_1^{meas} = \frac{m_T}{\sqrt{s}}(e^{y_3} + e^{y_4})$ and $x_2^{meas} = \frac{m_T}{\sqrt{s}}(e^{-y_3} + e^{-y_4})$, where y_3 refers to the photon

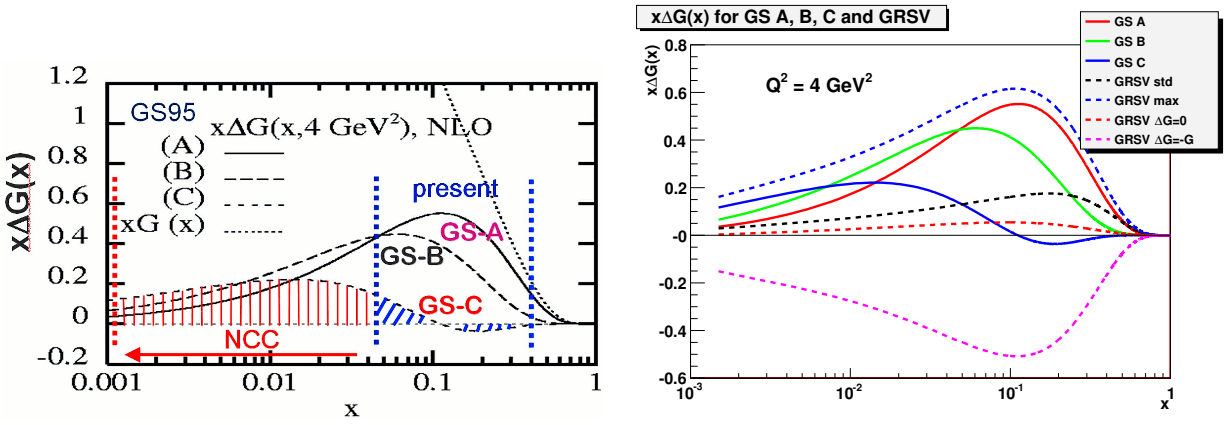

Figure 3.13: (left) Parameterizations with large contributions at low-x, such as GS-C cannot be distinguished without forward measurements. (right) Variety of parameterizations for ΔG Q^2=4 GeV^2.

and y_4 refers to the jet. M_T is taken as the p_T of the direct photon. Note that only the direction and not the momentum of the jet is used.

Since the error in the x-reconstruction for a LO analysis is $dx = \frac{xdp_T}{p_T} \oplus \frac{p_T e^{y_3} dy_3}{\sqrt{s}} \oplus \frac{p_T e^{y_4} dy_4}{\sqrt{s}}$, it is crucial to reconstruct the jet angle fairly well.[1] The angular resolution for reconstructed jets in the NCC as deduced from simulation is $\lesssim 0.1$ rad and contributes less than 10 % to the x resolution, which is below the amount expected from NLO radiative effects. In heavy ion collisions jets may be difficult to reconstruct cleanly, but leading particles (highest p_T particle in the NCC) provide a good proxy for the jet direction (Fig. 3.12).

3.3.6 Direct photon measurements and spin physics

Prompt photon production provides the most direct access to the gluon polarization, as it is dominated by the gluon-Compton process (85 % of the cross section). Present measurements indicate that ΔG is small in the kinematic range of the central region. However, these measurements are not sensitive to low-x and do not rule out even very large values of ΔG. For example, GS-C, a parameterization of the gluon structure that is consistent with all experimental data, has a very large value of ΔG, as illustrated in Fig. 3.13.

It is therefore essential to extend our measurements to low-x. The additional geometric acceptance with the addition of the NCC in the forward direction extends the measurement of the gluon polarization from $0.01 < x < 0.3$ down to about $x = 0.001$.

ΔG is extracted from measurements of the double spin longitudinal asymmetry (A_{LL}):

$$A_{LL} = \frac{\sigma_{++} - \sigma_{+-}}{\sigma_{++} + \sigma_{+-}} \approx \frac{\Delta g(x_1, Q^2)}{g(x_1, Q^2)} \otimes \frac{\Delta q(x_2, Q^2)}{q(x_2, Q^2)} \otimes \hat{a}_{LL}(s, t, u)$$

[1] In a γ-jet analysis the p_T would be determined from the photon's p_T.

for these various channels, where ++ denotes same sign helicity and +− denotes opposite sign helicity. A_{LL} is then connected to Δg in the context of pQCD.

As part of the work on this document we have estimated the sensitivity to A_{LL} for the prompt photon channel ($g + q \rightarrow \gamma + X$). The technique of estimating A_{LL} consists of calculating a weighting factor for A_{LL} on an event-by-event basis in a PYTHIA simulation. The PYTHIA prompt photon cross-section was checked to be in agreement with NLO pQCD calculations. The weighting factor w is expressed in the factorized form of A_{LL}:

$$w = r_g(x_1, Q^2) \otimes r_q(x_2, Q^2) \otimes \hat{a}_{LL}(s, t, u)$$

Here r is the ratio of $\Delta g(\Delta q)$ polarized density functions to the $g(q)$ unpolarized density functions and $\hat{a}_{LL}$ is the partonic asymmetry which is calculable in pQCD.

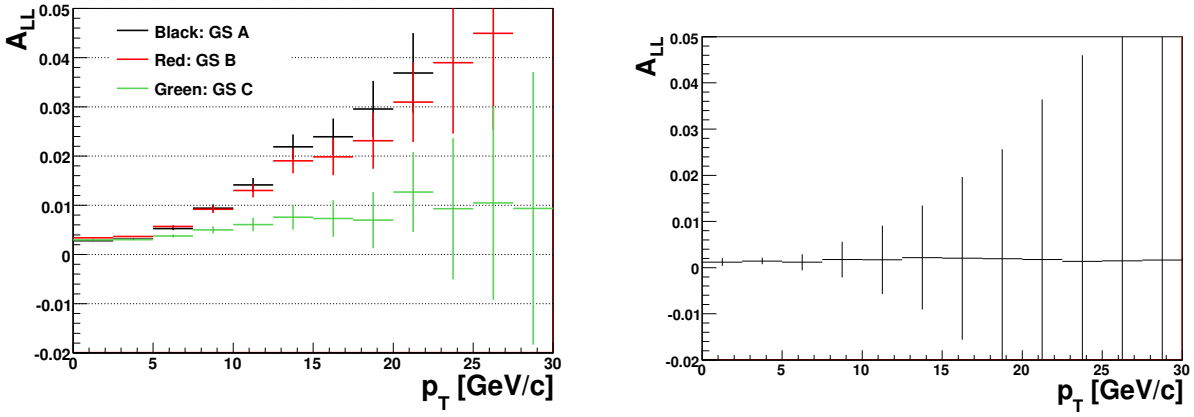

Figure 3.14: (left) A_{LL} for reconstructed prompt photons in the NCC for GS-A,B,C. (right) A_{LL} for prompt photons in the central arms for GS-C. Statistics are for running p+p with one NCC for 12 weeks at 500GeV and with 70 % polarization.

The estimated sensitivity to A_{LL} is shown in Fig. 3.14. We find that GS-C is clearly above 0, in contrast to central arm measurements. The addition of the NCC then gives us the possibility of testing parameterizations of the gluon structure function with large contributions at low-x. The photons have been reconstructed as described earlier, but dilution due to background is not included in the error bars. Further studies are being conducted on the isolation cuts to optimize the signal to background ratio.

3.3.7 π^0 summary

The NCC opens a new frontier for π^0 based studies with PHENIX at RHIC. It has a π^0 acceptance that exceeds the acceptance of the present PHENIX calorimeters by at least a factor of five, and significantly extends the rapidity range of π^0 studies in PHENIX. The new approach to measuring high p_T π^0s proposed for the NCC allows also to extend the p_T range for nuclear modification studies which would otherwise be impossible even when luminosity

reaches the expected RHIC-II levels. While limitations to the transverse momentum reach in the central arm are set by the central EMC tower size, the p_T reach in NCC is expected to reach 30 GeV/c, limited mainly by the expected luminosity.

3.4 The χ_C

In this study we present an R_{AA} measurement for the χ_C given realistic backgrounds and detector response. The muon arms provide the measurement of the J/ψ via its decay to dimuons. For our purposes the Level-2 dimuon trigger in the muon arms is sufficient in determining whether there is a dimuon event in the rapidity of interest.

We began by generating HIJING background events for each collision type (p+p, d+Au, Au+Au) in varying centrality classes. The signal was generated using a combination of χ_C and J/ψ single particle generators to give us an appropriate mixture (4:6) of J/ψs from the feed-down of χ_C and directly produced J/ψ. To get large enough statistics at high p_T, we used a flat (p_T, y) distribution which was then rescaled to expected yields for one run at RHIC-II luminosity. The p_T and rapidity ranges studied are $0 < p_T < 10\,\mathrm{GeV}/c$ and $1 < \eta < 3$. The transverse momentum range was split into 20 bins, and the rapidity into 3 bins. The background to the χ_C was assumed to arise from 1) directly produced J/ψs combined with photons; 2) J/ψ from χ_C combined with random photons; 3) a background under the J/ψ coming from random high mass muon pairs as measured in the present spectrometer and improved by a factor of 2.5 because of the improvement in resolution and hadron rejection from the FVTX. The first two were taken directly from the simulation, the last was taken from a combination of the present J/ψ data and studies by the FVTX.

Once the signal and background files were generated they were passed through the GEANT-3 package (PISA). The signal and background files were then merged at the raw event level, and passed though the detector response stage to produce simulated DSTs. The merged events were then subjected to pattern recognition and reconstruction routines. Output DSTs were made for further analysis. The samples used are summarized in table 3.5.

Table 3.5: Sample size for the χ_C study.

Interaction	Centrality	Events per bin of η and p_T
p+p	minbias	10,000
d+Au	minbias	10,000
d+Au	b=0-5, 0-40%	10,000
Au+Au	each centrality	5,000

In order to make a measurement on the process $\chi_C \rightarrow J/\psi + \gamma$, it is necessary that both the dimuon pair and primary photon be within the acceptance of the detector. Once the J/ψ from a χ_C is accepted in the muon spectrometer there is about a 70 % chance of the primary photon being in the acceptance of the NCC. We have a further photon reconstruction

efficiency of around 80 % for the low energy (typically 1 GeV) photons expected from a χ_C decay in p+p events, with the efficiency dropping with multiplicity. We apply several cuts to the photons before constructing an invariant mass. In order to select electromagnetic showers, a χ^2 <10 cut was applied where χ^2 is the sum of the longitudinal and transverse χ^2s as determined from the pads. The photons were required to have an $E_\gamma > 500\,\mathrm{MeV}$ in order to suppress the background from low energy tracks. A minimum angle cut between each muon and the photon was necessary due to the clustering algorithms used. Photons that are very nearly collinear with the muons are lost, because the muon track absorbed the photon in the clustering algorithm. This effect, which is not present in mixed events, leads to a dip in the distribution immediately below the χ_C after background subtraction. The combinatorial background shape is found by mixed event background subtraction in which we take a J/ψ from the current event and pair it with NCC tracks from previous minimum bias events. The mixed events are normalized to a region above 800 MeV, or about 3 σ above the χ_C peak. These yields were then obtained and renormalized to the p_T and y spectra from PYTHIA assuming binary scaling, together with the suppression factors measured in the PHENIX detector for the J/ψ. The yields were finally scaled to the expected luminosities for RHIC-II.

We follow the standard practice of looking at the difference between the J/ψ+γ invariant mass and the J/ψ mass, since this eliminates much of the resolution smearing of from the muon measurement. The width of our signal is then dominated by the energy resolution of the photons. Fig. 3.15 shows the foreground and mixed background overlaid along with the resulting subtracted invariant mass distributions for p_T = 6, 7, and 8 GeV, in p+p, d+Au minimum bias, d+Au central (0-20 %), and Au+Au mid-central (30-40 %) collisions. At centralities above 30% in AuAu collisions, the systematics in our background subtraction become large and will require further study possibly requiring the use of the strip detectors PI1 and PI2.

3.4.1 χ_C $\mathbf{R}_{AA}$

The suppression of charmonium, which originally was supposed to be a clear indication of deconfinement, presents a puzzle to the heavy ion community. Prior to the publication of the data from PHENIX, one of the main expectations was that the J/ψ would be completely suppressed in Au+Au collisions at RHIC due to the higher energy densities available as compared to the SPS. However the suppression pattern seen at RHIC was measured to be similar to that as seen at CERN [23].

Results in the last few years from the lattice community indicate that a correlation between the charm pair of a J/ψ survives above the critical temperature, while the χ_C and ψ' should dissociate at a temperature near T_C [18]. One simple explanation of the RHIC results put forward by Karsch, Kharzeev and Satz [24] is that since much of the J/ψ yield comes from the decay of the χ_C and ψ', all χ_Cs and ψ's should be melted both at CERN and at RHIC, and that the melting point of the J/ψ is higher than is reached at RHIC. In addition regeneration also may come into effect, particularly if charm is significantly enhanced [25]. It becomes critical then to actually measure not only the J/ψ, but also other

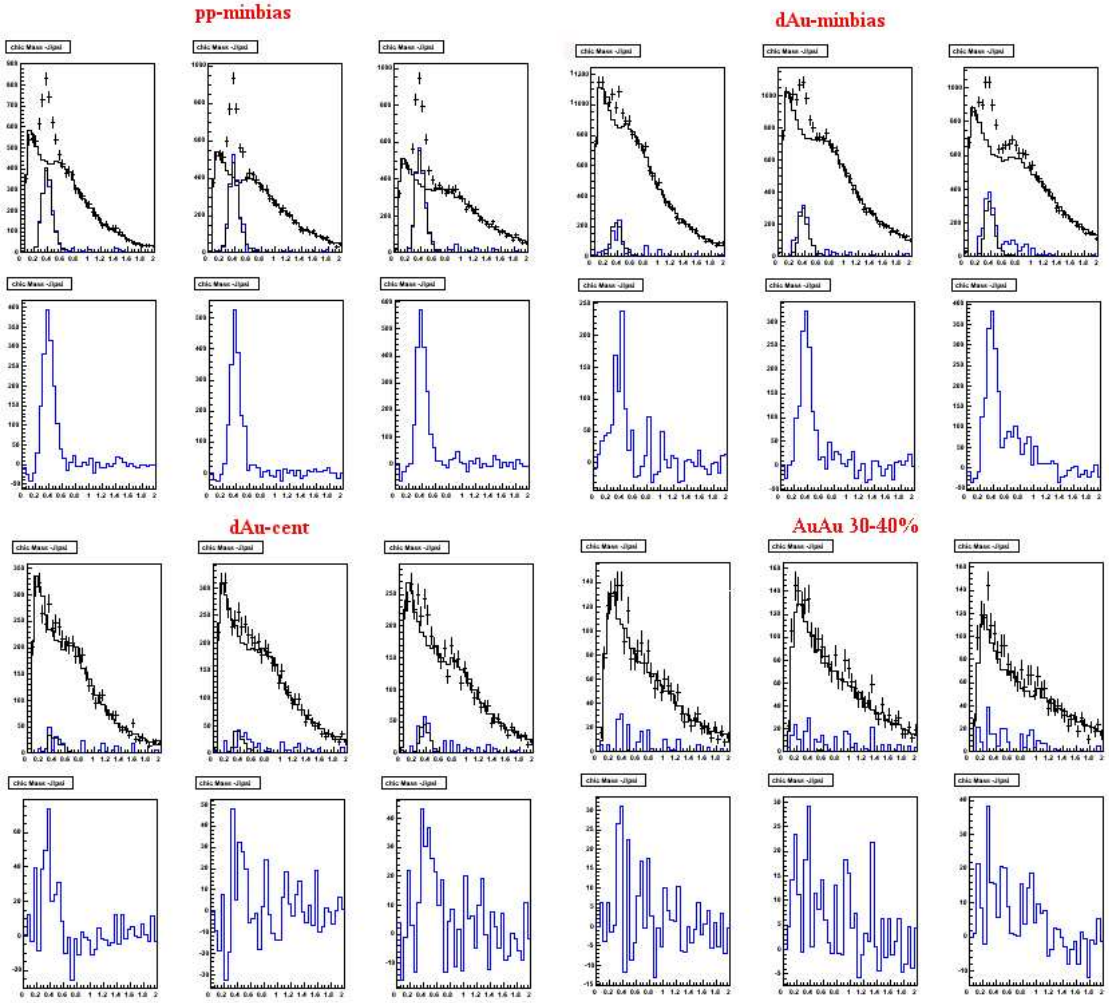

Figure 3.15: The χ_C reconstructed signal. Top and 3rd rows show the J/$\psi + \gamma$ invariant mass, the normalized mixed background and the signal after subtraction. The 2nd and 4th rows show the subtracted signal. The upper left is for p+p collisions, for p_T = 6, 7 and 8 GeV. The upper right is the same for d+Au minimum bias collisions. Bottom left is for d+Au central, and bottom right for the Au+Au 30-40 % centrality bin.

particles with different screening lengths (melting temperatures) – in particular the χ_C since it is responsible for a large fraction of the J/ψs seen.

The first and perhaps most pressing question which one would immediately ask is whether J/ψ suppression was entirely due to the suppression of the χ_C. In this case one would expect the χ_C to be seen at it normal level with respect the J/ψ in p+p, d+Au, and peripheral Au+Au collisions, then to be rapidly suppressed as a function of N_{part} until energy densities comparable to those in central Pb+Pb collisions at CERN were reached at RHIC. Using a simple Bjorken model for the energy densities this would mean that the χ_C should be almost *completely suppressed* at RHIC in collisions where N_{part} is greater than 100 participants.

Fig. 3.16 shows the accuracy with which we can measure the N_{part} dependence of the

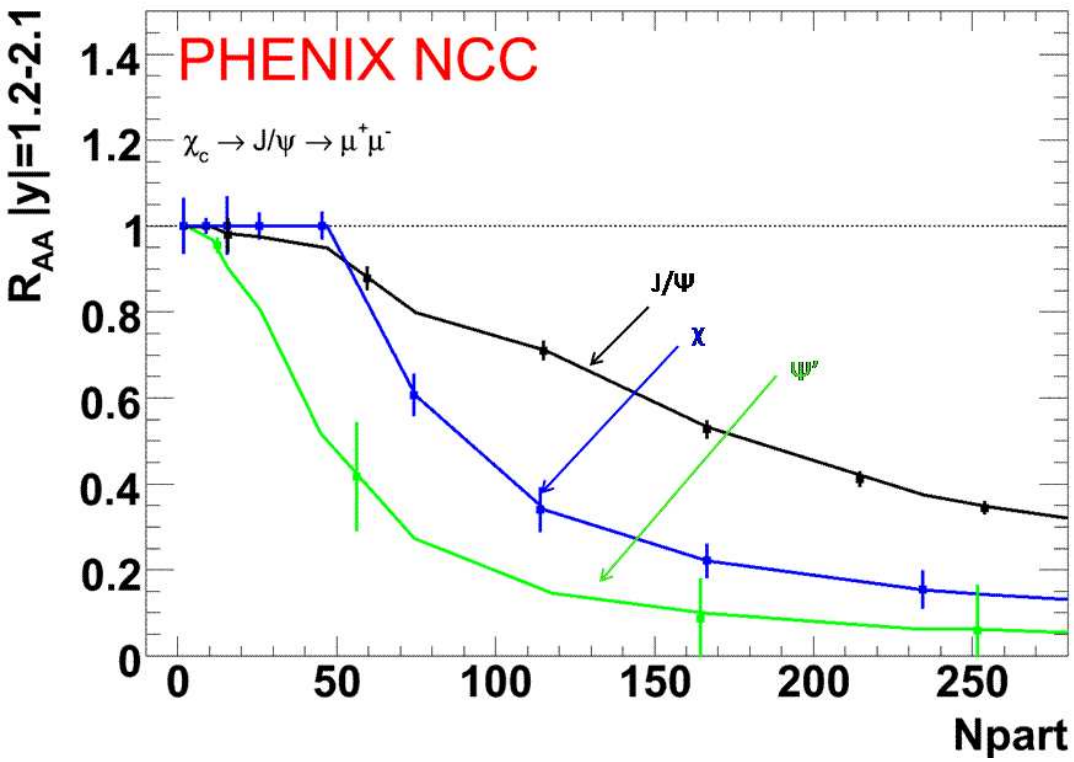

Figure 3.16: R_{AA} of χ_C vs N_{part}, where the error bars reflect the statistics for one run at RHIC-II luminosity for the χ_C. The location of the points is taken from a model of as explained in the the text. Also shown for comparison are the model predictions for the J/ψ and ψ'.

χ_C R_{AA}. The suppression pattern shown is taken from a model motivated by the Karsch, Kharzeev and Satz conjecture where the dissociation temperature of $1.16\,T_C$ is assumed for the χ_C and ψ'. A Glauber calculation is used to obtain the energy density. Remnants of the χ_C are still visible for central events because the temperature on the periphery of the collision is assumed to be below that of the dissociation temperature of the χ_C. In this model, if the energy density is above the critical density in a $1\,fm^2$ area then the state is assumed to be dissociated. One will clearly be able to differentiate between the case where the suppression pattern of the χ_C is identical to that of the J/ψ or that where the χ_C is enhanced to the extent which may explain the similarity of the CERN and RHIC measurements.

Fig. 3.17 shows R_{AA} as a function of p_T. The p_T dependence is important to discriminate between models since lower p_T states would tend to experience the medium differently and show a different magnitude from effects such as dissociation, screening, and coalescence.

3.4.2 χ_C summary

The suppression of charmonium has played an important part in the search for deconfinement. The NCC together with the PHENIX muon spectrometer will make it possible to

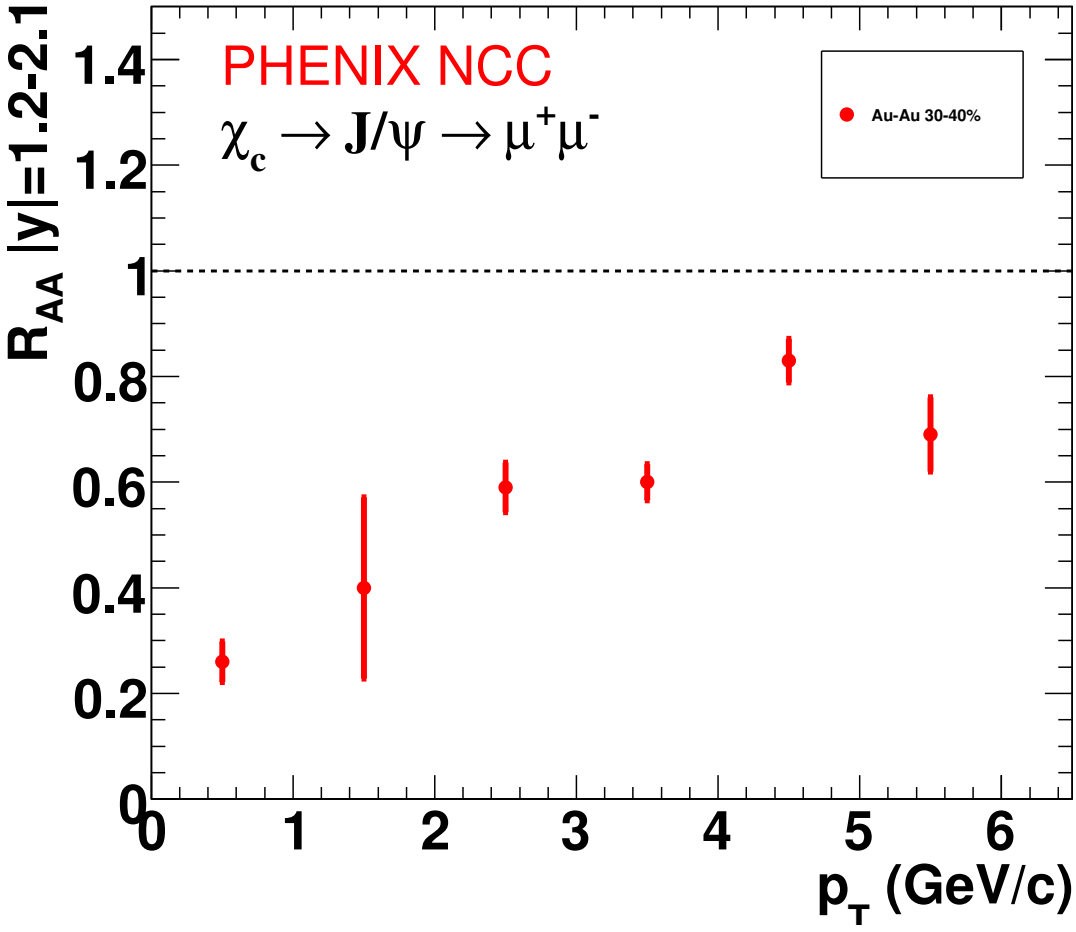

Figure 3.17: R_{AA} of the χ_C as a function of p_T for centrality 30-40 % Au+Au collisions.

measure χ_C production in heavy ion collisions for the first time. R_{AA} will be measured to better than 0.1, i.e., with sufficient precision to distinguish between a model in which the χ_C and ψ' account for all the suppression of the J/ψ at RHIC and and CERN, and the case in which the χ_C is suppressed similarly to the J/ψ. A variety of theoretical possibilities exist to explain the suppression of charmonium, including some which have not been mentioned here. The measurement of the suppression of the χ_C as a function of centrality and p_T using the NCC will be crucial to disentangling the various effects and provide an understanding of the relationship between the suppression of charmonium and deconfinement.

Chapter 4

Summary

We have presented in this report our simulated performance for the NCC.

- We have shown the performance of the NCC as a non-projective tracking calorimeter. Efficiencies for finding and identifying electromagnetic showers, while not completely independent of angle, momentum, or multiplicity, are reasonably uniform, and well within the standard correction methods used in PHENIX (Figure 2.8).

- The NCC opens a new frontier for π^0 based studies with PHENIX at RHIC. It has a π^0 acceptance that exceeds the acceptance of the present PHENIX calorimeters by at least a factor of five, and significantly extends the rapidity range for π^0 studies in PHENIX. The new approach to measuring high p_T π^0s proposed for the NCC allows also to extend the p_T range for nuclear modification studies to a range which would otherwise be impossible even with RHIC-II luminosities. While limitations to the transverse momentum reach in the central arm are set by the central EMC tower size, the p_T range in the NCC is expected to reach $30\,\mathrm{GeV}/c$, and is limited mainly by the expected luminosity (Fig. 3.3.3). From the measurements of the π^0 we are able to then extract direct photons and hence this paves the way for photon-jet measurements in conjunction with other detectors, as well as the measurement of the gluon contribution to the proton spin at low $x \sim 10^{-3}$.

- The study of charmonium suppression via the χ_C is made possible for the first time (Fig. 3.16). We also note that this is perhaps the only possibility for the measurement of the χ_C in heavy ion collisions at any machine for the foreseeable future, which makes it a unique opportunity in terms of the critical new information that this measurement brings to the question of deconfinement.

The NCC will extend the capabilities of the PHENIX detector significantly, by extending the acceptance of electromagnetic calorimetry to higher rapidity, opening up the horizons of rare physics – such as direct photons, photon-jets, and the χ_C, at reasonable event rates.

List of Figures

List of Tables

References

[1] **PHENIX** Collaboration, 2007. Technical Design Report of the Forward Silicon Vertex Tracker (internal report).

[2] **PHENIX** Collaboration, M. Chiu `nucl-ex/0701031`.

[3] **PHENIX** Collaboration, K. Adcox *et. al. Nucl. Phys.* **A757** (2005) 184–283 [`nucl-ex/0410003`].

[4] **PHENIX** Collaboration, K. Adcox *et. al. Phys. Rev. Lett.* **87** (2001) 052301 [`nucl-ex/0104015`].

[5] **PHENIX** Collaboration, K. Adcox *et. al. Phys. Lett.* **B561** (2003) 82–92 [`nucl-ex/0207009`].

[6] **PHENIX** Collaboration, S. S. Adler *et. al. Phys. Rev. Lett.* **96** (2006) 032302 [`nucl-ex/0508019`].

[7] **PHENIX** Collaboration, S. S. Adler *et. al. Phys. Rev. Lett.* **95** (2005) 202001 [`hep-ex/0507073`].

[8] **PHENIX** Collaboration, S. S. Adler *et. al. Phys. Rev. Lett.* **94** (2005) 232301 [`nucl-ex/0503003`].

[9] **PHENIX** Collaboration, S. S. Adler *et. al. Phys. Rev. Lett.* **93** (2004) 202002 [`hep-ex/0404027`].

[10] **PHENIX** Collaboration, S. S. e. a. Adler *Phys. Rev. Lett.* **91** (2003) 072303 [`nucl-ex/0306021`].

[11] **PHENIX** Collaboration, S. S. Adler *et. al. Phys. Rev. Lett.* **91** (2003) 241803 [`hep-ex/0304038`].

[12] **PHENIX** Collaboration, A. Adare *et. al. (to be published)* (2008) [`arXiv:0801.4020`].

[13] R. Wigman, *Calorimetry, Energy Measurement in Particle Physics*. Oxford Science Publications, Oxford University Press, Great Clarendon Street, Oxford OX2 6DP, 2000.

[14] **PHENIX** Collaboration, A. Adare *et. al. (to be published)* (2008) [`arXiv:0801.1665`].

[15] F. Arleo arXiv:0706.1848.

[16] **PHENIX** Collaboration, A. Adare *et. al. Phys. Rev. Lett.* **98** (2007) 172301 [nucl-ex/0611018].

[17] **PHENIX** Collaboration, A. Adare *et. al.* arXiv:0801.0220 [nucl-ex].

[18] S. Datta, F. Karsch, P. Petreczky and I. Wetzorke *Phys. Rev.* **D69** (2004) 094507 [hep-lat/0312037].

[19] L. E. Gordon and W. Vogelsang *Phys. Rev.* **D48** (1993) 3136.

[20] D. Florian and W. Vogelsang *Phys. Rev.* **D71** (2005) 114004.

[21] **WA98** Collaboration, M. M. Aggarwal *et. al. Phys. Rev.* **C67** (2003) 014906 [nucl-ex/0210002].

[22] J. Jalilian-Marian nucl-th/0703069.

[23] **PHENIX** Collaboration, S. S. Adler *et. al. Phys. Rev.* **C69** (2004) 014901 [nucl-ex/0305030].

[24] F. Karsch, D. Kharzeev and H. Satz *Phys. Lett.* **B637** (2006) 75–80 [hep-ph/0512239].

[25] R. L. Thews *Nucl. Phys.* **A783** (2007) 301–308 [hep-ph/0609121].